NOVEL OPTICAL SCANNER USING PHOTODIODES ARRAY FOR TWO-DIMENSIONAL MEASUREMENT OF LIGHT FLUX DISTRIBUTION

By

YEW TIONG KEAT

A thesis submitted to the
Department of Electrical and Electronic Engineering,
Faculty of Engineering and Science,
Universiti Tunku Abdul Rahman,
in partial fulfillment of the requirements for the degree of
Master of Engineering and Science
July 2011

Universiti Tunku Abdul Rahman
July 2011

ABSTRACT

NOVEL OPTICAL SCANNER USING PHOTODIODES ARRAY FOR TWO-DIMENSIONAL MEASUREMENT OF LIGHT FLUX DISTRIBUTION

Yew Tiong Keat

A light flux mapping system or known as optical scanner which is capable of acquiring light flux distribution pattern on a two-dimensional flat surface of many types of light source has been designed and constructed. The special features of the novel optical scanner are its high resolution measurement with relatively fewer sensors, fast speed and can be used for precise calibration of any light source. In the design of the optical scanner, 25 photodiodes with a photo-sensitive area of 1 cm^2 were arrange closely to each other and fixed to an aluminum holder. By moving the row of photodiodes in a direction, it can scan and acquire flux distribution data in two-dimensional measurement surface plane. The resulting scanner was fast enough to perform scanning and recording of light irradiance over a test plane area of 1125 cm^2 within a time period of 5 seconds. The optical scanner is used to study the solar flux distribution of different types of artificial light source, the image reflected by mirror with different dielectric thickness and finally its performance was evaluated with measurement of highly uniform sunlight.

ACKNOWLEDGEMENT

First and foremost, I would like to take this opportunity to express my sincere appreciation and deepest gratitude to my supervisor, Dr. Chong Kok Keong, for his guidance, invaluable advice, understanding and considerations on my works. I was able to gain a lot of experiences, skills and knowledge from him.

I wish to express my gratitude to Dr. Lau Sing Liong, my co-supervisor. He had provided me continuous guidance, directions and advice when I was conducting my works. I would also wish to indicate special gratitude and deepest thankfulness to my research's partners, Jessie Siaw Fei Lu, Wong Chee Woon and Chong Yee How, for their assistances. Furthermore, I would like to appreciate to none forgetting all of the lab officers and lab assistants, especially Mr. Ho Kok Wai. They always give me support, encouragement, advice, technical expertise and experiences.

To my beloved family, appreciate for the encouragement and mentally support throughout the duration of my study.

APPROVAL SHEET

This thesis entitled " **NOVEL OPTICAL SCANNER USING PHOTODIODES ARRAY FOR TWO-DIMENSIONAL MEASUREMENT OF LIGHT FLUX DISTRIBUTION** " was prepared by YEW TIONG KEAT and submitted as partial fulfillment of the requirements for the degree of Master of Engineering and Science at Universiti Tunku Abdul Rahman.

Approved by:

____

(Dr. CHONG KOK KEONG)
Date:……………....
Supervisor
Department of Electrical and Electronic Engineering
Faculty of Engineering and Science
Universiti Tunku Abdul Rahman

____

(Dr. LAU SING LIONG)
Date:……………....
Co-supervisor
Department of Electrical and Electronic Engineering
Faculty of Engineering and Science
Universiti Tunku Abdul Rahman

FACULTY OF ENGINEERING AND SCIENCE

UNIVERSITI TUNKU ABDUL RAHMAN

Date: 18 July 2011

SUBMISSION OF THESIS

It is hereby certified that **YEW TIONG KEAT** (ID No: **07UEM08774**) has completed this thesis entitled "**NOVEL OPTICAL SCANNER USING PHOTODIODES ARRAY FOR TWO-DIMENSIONAL MEASUREMENT OF LIGHT FLUX DISTRIBUTION**" under the supervision of Dr. CHONG KOK KEONG (Supervisor) from the Department of Electrical and Electronic Engineering, Faculty of Engineering and Science, and Dr. LAU SING LIONG (Co-Supervisor) from the Department of Electrical and Electronic Engineering, Faculty of Engineering and Science.

I understand that University will upload softcopy of my thesis in pdf format into UTAR Institutional Repository, which may be made accessible to UTAR community and public.

Yours truly,

____

(YEW TIONG KEAT)

DECLARATION

I hereby declare that the dissertation is based on my original work except for quotations and citations which have been duly acknowledged. I also declare that it has not been previously or concurrently submitted for any other degree at UTAR or other institutions.

Name : Yew Tiong Keat

Date : 18 July 2011

TABLE OF CONTENTS

	Page
ABSTRACT	ii
ACKNOWLEDGEMENT	iii
APPROVAL SHEET	iv
SUBMISSION OF THESIS	v
DECLARATION	vi
TABLE OF CONTENTS	vii
LIST OF TABLES	x
LIST OF FIGURES	xi
LIST OF ABBREVIATIONS	xvii

CHAPTER

1.0	INTRODUCTION		1
	1.1	Research Background	1
	1.2	Research Objective	4
	1.3	Thesis Overview	4
2.0	LITERATURE REVIEW		5
	2.1	Direct Measurement Method	5
	2.2	Simulation Method	18
3.0	METHODOLOGY		21

3.1	The Optical Scanner		21
	3.1.1	Photodiode	22
	3.1.2	Stepper Motor and Microstep Driver	23
	3.1.3	Microcontroller	25
	3.1.1	Multiplexer	26
	3.1.1	Operational Amplifier	27
	3.1.1	User Interface Program	28
3.2	Optical Scanner Design		29
3.3	Operating Procedure		43

4.0	EXPERIMENTAL SETUP and RESULT			46
	4.1	Experimental Setup		46
		4.1.1	Artificial Light Sources	46
		4.1.2	Sunlight	47
		4.1.3	Solar Flux Distribution for Different Thickness of Mirror	48
	4.2	Results		50
		4.2.1	Artificial Light Sources	50
		4.2.2	Sunlight	53
		4.2.3	Solar Flux Distribution for Different Thickness of Mirror	55

5.0	DISCUSSION and CONCLUSION			61
	5.1	Discussion		61
		5.1.1	Trade-offs in terms of Cost, Speed, Accuracy	61

and Type of Light Source
5.1.2 Potential for 3-D Measurements 63
5.1.3 Measurement of Light Flux of Very High Concentration 64
5.2 Conclusion 64

REFERENCES 66
APPENDICES

A TL084 OPERATIONAL AMPLIFIERS 70
B HCF4053B ANALOG MULTIPLEXER 73
C PIC18F4550 44-PIN USB MICROCONTROLLERS 76
D SLSD-71N5 PLANAR PHOTODIODE 82
E Novel Optical Scanner Using Photodiodes Array for Two-Dimensional Measurement of Light Flux Distribution 83

LIST OF TABLES

Table		Page
5.1	Comparisons in terms of cost, speed, accuracy and type of light source among three different possible methods of acquiring the light flux distribution map.	62

LIST OF FIGURES

Figure		Page
2.1	Solar Simulator Uniformity Mapper.	6
2.2	Intensity map of test data collected by Solar Simulator Uniformity.	6
2.3	Schematic of the LS–CCD method applied to a planar receiver in the reflection mode.	7
2.4	The left picture shows the target package in operation in the EURODISH while the picture on the right shows the target package on ground.	8
2.5	The moving bar is a compound of non-cooled white target and non-cooled HFM calorimeters array. The bar passes in front of the receiver aperture obtaining two measurements of the incident power.	9
2.6	Schematic of the fluxmeter using an integrating sphere and a photo-sensor (1) area of first inpact S_F, (2) area of measurement, (3) photo-sensor.	10
2.7	Measurement of the light power impinging on the lens.	11
2.8	Scheme of the SCCAN technique for the optical characterization of heliostats in a central tower system.	12

2.9	General model of the radiometer with two coupled integrating spheres. G_1 irradiance in the first sphere; G_2 irradiance in the second sphere; (w_{pd}) photodetector window for irradiance measurements.	13
2.10	Arrangement of a solar furnace and an apparatus measuring target temperature.	14
2.11	Optical system of the brightness pyrometer.	15
2.12	(a) Flat plate calorimeter and (b) cross-sectional diagram showing the coordinate axes used in the theoretical model.	16
2.13	PARASCAN flux scanner mounted on the EuroTrough prototype collector, and the two sensor parts (below right, zoomed in).	17
2.14	Photo of monitoring device attached to absorber. The photo diode is situated at the end of the sliding device.	18
3.1	Schematic diagram to show the major components of the novel optical scanner.	22

3.2	Diagram of solderable planar photodiode with dimension.	23
3.3	Geared type stepper motor used in the optical scanner with gear ratio of 1:7.2.	24
3.4	Mircrostep driver of stepper motor.	24
3.5	Pin diagram of microcontroller PIC18F4550.	25
3.6	HCF4053B triple 2-channel analog multiplexer.	27
3.7	Pin diagram of general purpose J-FET quad operational amplifiers TL084A.	28
3.8	Graphic user interface of optical scanner.	29
3.9	The arrangements of 4 of the photodiodes in the photodiodes array.	30
3.10	Schematic diagram to show the calculation of field of view of the photodiode.	32

3.11 Small cell representing the position and the area of each measurement during the scanning process. The square cells as shown in the above schematic diagram denote the positions at which the readings of light irradiance are acquired and subsequently sent to the microcontroller. During the process of data acquisition, the readings are collected simultaneously for all the photodiodes arranged in the same row and then the scanner is shifted to the next row after the readings are stored. 35

3.12 Pryheliometer that measure normal incident sunlight. 36

3.13 Calibration graph for one of the photodiodes installed on the measurement array. 38

3.14 Photoconductive mode: reverse bias, has "dark" current, higher noise (Johnson + shot), high speed applications. 39

3.15 Photovoltaic mode: zero bias, no "dark" current, low noise (Johnson), precision applications. 40

3.16 The overall architecture of the photodiodes and the accompanying electronic circuit. 41

3.17 Flow chart of the optical scanner operation. 44

4.1	Experimental setup of the optical scanner with light source consisting of motorcycle xenon headlamps of 35 W each.	47
4.2	Experiment setup of Optical Scanner.	48
4.3	Prototype of Non-Imaging Planar Concentrator (NIPC) with all the mirrors blocked with black plastic cover except the specimen mirror. The specimen flat mirror with different thickness has been tested under the sun.	49
4.4	Light flux distribution of the first artificial light source consisted of three motorcycle xenon headlamp of 35 W each: (a) picture taken by a CCD camera, (b) contour map plotted by the optical scanner. The light source utilized in is consisted of three motorcycle xenon headlamp with 35 W each. The distance between the light source and the scanner was fixed at 50 cm. All the lamps used during the measurement were reasonably new with a total operating time of less than 5 hours.	51

4.5 Light flux distribution of the second artificial light source comprised of three commercial xenon lamps of 20 W each: (a) picture taken by a CCD camera, (b) contour map plotted by the optical scanner. The light source utilized was consisted of three commercial xenon lamps of 20 W each. The distance between the light source and the scanner was fixed at 50 cm. All the lamps used during the measurement were reasonably new with a total operating time of less than 5 hours. 52

4.6 Light flux distribution of sunlight with a direct normal irradiance of 752 W/m^2. 54

4.7 Flux maps show the solar flux distribution of image reflected by mirror with different glass thickness of (a) 3mm, (b) 4mm, (c) 5mm, (d) 6mm. 56

4.8 Flux maps from optical simulation show the solar flux distribution of image for a single mirror. 60

LIST OF ABBREVIATIONS

LEDs	Light Emitting Diodes
CCD	Charge-coupled device
I	Light irradiance
ADC	Analog-to-Digital Converter
LSB	Least Significant Bit
USB	Universal Serial Bus
NIPC	Non-Imaging Planar Concentrator
CPV	Concentrator Photovoltaic

CHAPTER 1

INTRODUCTION

1.1 Research Background

The determination of solar flux intensity distribution on the photovoltaic or thermal receiver is essential during the alignment of the optical components of the concentrator system. For concentrating photovoltaic systems, it is well known that a non-uniform light distribution on the cells can negatively affect the systems' electrical performance and can even cause failure in some cells due to local overheating. A periodic monitoring of the light intensity distribution on the system receiver is also highly desirable as it could offer important information on the effective optical efficiency of the system (Parretta e*t al.*, 2006).

Solar simulators and supplemental lighting systems are widely used in research institutes and industries for indoor applications due to their ready availability, consistency of supply, and their output not being affected by the weather. For photovoltaic research, solar simulators using xenon arc lamps are widely employed to characterize the performance of solar cells by plotting I-V curves resulting from the simulated sunlight. For horticulture, the use of supplemental lighting systems has significantly increased recently as more growers are interested in shortening the time needed for their crops to reach maturity, and sometimes to increase annual yield through continuous plantings throughout the winter season (Both e*t al.*, 2002).

In the aforementioned applications, the uniform illumination emanating from the light source in either solar simulator or supplemental lighting system is the major concern to obtain the desired outcome. Light uniformity of the solar simulator is one of the key factors to obtain accurate measurements of I-V curves for the tested solar cell (Vandenberg e*t al.*, 1993). Any spatial variation of light irradiance will affect the performance of solar cells and hence deteriorate the accuracy and consistency of the test result. On the other hand, a high degree of light uniformity is also required from a supplemental lighting system to ensure the consistency in crop yield throughout a growing area. The supplemental lighting system normally consists of light source, e.g. light bulb, tube lamps or arrays of Light Emitting Diodes (LEDs), etc., and optical components, e.g. reflectors, collimators, filters etc. The main objective of the optical components is to project the light so that the irradiance from the light source can be uniformly distributed across the crops. The uniform exposure of irradiance over the crops is to avoid uneven growth and variable quality. The uniformity information can be used to determine the maximum allowable lamp spacing across the growing area. Therefore, uniformity calibration of the light source across the illuminated area in the aforementioned applications is important to quantify the quality of the light source.

In common practice, the uniformity tester utilizes a two-dimensional array of solar cells to assess the uniformity of irradiance on the tested surface, which is a rather expensive and complicated solution (PV Measurements Inc, 2009). In the design of a tester, solar cells are arranged in an $m \times n$ array that covers a square or rectangular plane surface. By exposing an array of solar cells to the light source, a current proportional to the irradiance level will be generated by each solar cell. The signal conditioning circuitry then produces signals that are proportional to the output current and that are transmitted to the data acquisition equipment and subsequently to the computer. Finally, the computer performs data interpretation to provide a graphical display of the uniformity of the light source in a two-dimensional space. For the measurement over a wider surface plane, more solar cells are needed for the uniformity tester to achieve the same resolution. The size of the sensor helps to determine the resolution of the measurement system. The sensor is unable to detect the spatial non-uniformity of light irradiance occur within the sensor's sensitive area because the output of a light sensor is basically the average irradiance of the light falling in its sensitive area. Hence the larger the size of a sensor used in a measurement system, the lower the ability of the measurement system to detect the non-uniformity profile of any light source. For a study or test requiring a high degree of uniformity from the light source, a reasonably small size sensor will be needed. However, this will indirectly increase the cost and complexity of the uniformity tester design.

The aim of this thesis is to present a design and construction of a novel uniformity tester called an optical scanner that is able to measure the distribution of light irradiance over a plane surface with reasonably high resolution and using a much simpler design (Chong and Yew, 2011).

1.2 Research Objective

There are three objectives of this work:

1. To design and construct a novel optical scanner for measuring solar flux distribution.

2. To evaluate the performance of the optical scanner using different types of light source.

3. To study and analyze the uniformity of reflected sunlight from mirrors of different thickness using the optical scanner.

1.3 Thesis Overview

The organization of the thesis is as follow: Chapter 1 of this thesis gives a general idea of the research and clarifies the research objectives. Chapter 2 gives the literature about the various types of the evaluation method of light flux distribution. In Chapter 3, the design and construction of the optical scanner is discussed in detail. Experimental setups and results of the optical scanner are discussed in Chapter 4. Chapter 5 ends the thesis with the discussion and conclusion.

CHAPTER 2

LITERATURE REVIEW

To understand the light flux distribution of solar collector and solar simulator, studies are carried out with either direct measurement or simulation method. Different types of direct measurement technique and simulation study are discussed in the following text.

2.1 Direct Measurement method

Currently, there is a commercial Solar Simulator Uniformity Mapper in the market developed by PV measurements Inc. (2009). The uniformity tester uses an array of solar cells to assess the uniformity of light on its surface. The 8 x 8 array of solar cells covers a 21 cm x 21 cm plane, enabling the system to test solar simulators with a 21 cm x 21 cm illumination area. A 6 x 6 subset of these cells can be used to assess the uniformity of light from simulators with a 15.6 cm x 15.6 cm illumination area. Figure 2.1 shows the Solar Simulator Uniformity Mapper and Figure 2.2 shows the intensity map of test data collected by Solar Simulator Uniformity Mapper.

.

Figure 2.1: Solar Simulator Uniformity Mapper (PV Measurements Inc, 2009).

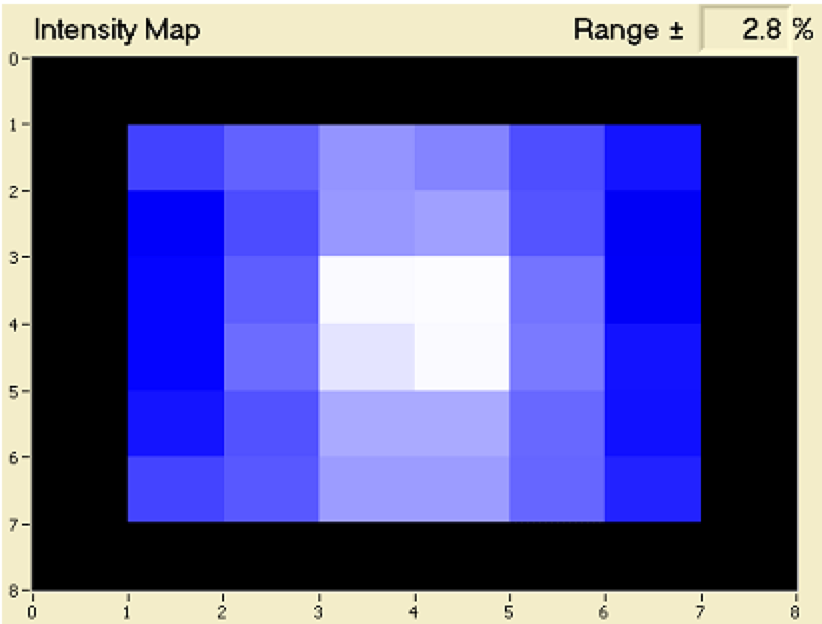

Figure 2.2: Intensity map of test data collected by Solar Simulator Uniformity Mapper (PV Measurements Inc, 2009).

Antonio Parretta *et al.* (2006) described methods for evaluating the light intensity distribution on receivers of concentrated radiation systems. They based on the use of Lambertian diffusers in placed of the illuminated receiver and on the acquisition of the scattered light, in reflection or transmission mode, by a charge-coupled device (CCD) camera. The spatial distribution of intensity radiation is then numerically derived from the received image of the proprietary code. Figure 2.3 shows the schematic of the LS–CCD method applied to a planar receiver in the reflection mode.

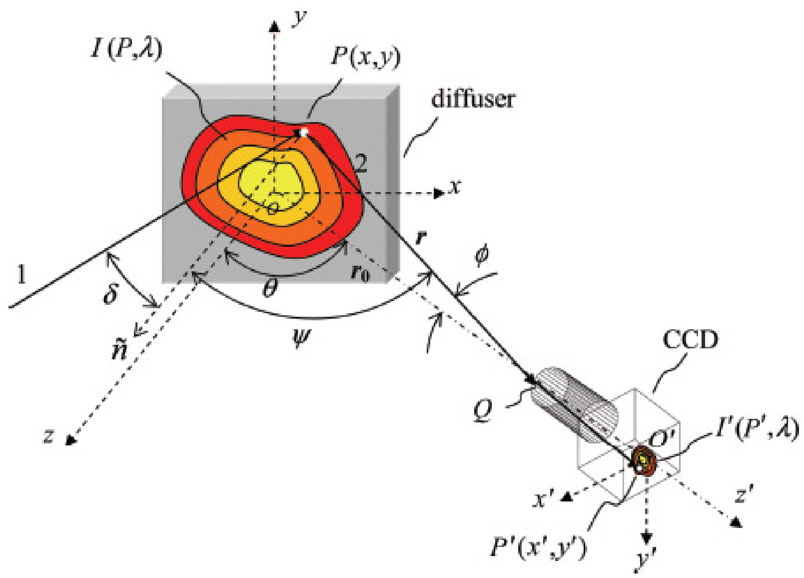

Figure 2.3: Schematic of the LS–CCD method applied to a planar receiver in the reflection mode (Antonio Parretta *et al.*, 2006).

Steffen Ulmer *et al.* (2002) built and operated a flux mapping system able to measure the flux distribution of dish/Stirling systems in planes perpendicular to the optical axis at the Plataforma Solar de Almerı´a (PSA). It used the indirect measuring method with a water-cooled Lambertian target placed in the beam path and a CCD-camera mounted on the concentrator taking images of the brightness distribution of the focal spot. The calibration is made by calculating the total power coming from the dish and relating it to the integrated gray value over the whole measurement area. The equipment consists of a target package with a water-cooled, moveable target plate placed in the beam path, a CCD-camera fixed to the concentrator and a computer on the ground that controls target plate positioning and picture acquisition. Figure 2.4 shows the target package in operation in the EURODISH and the target package on ground.

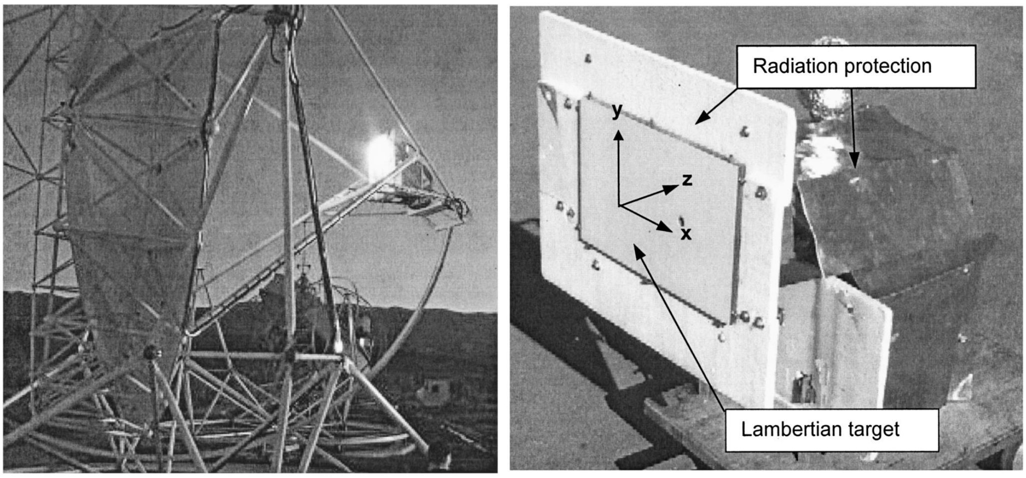

Figure 2.4: The left picture shows the target package in operation in the EURODISH while the picture on the right shows the target package on ground (Steffen Ulmer *et al.*, 2002).

J. Ballestrin and R. Monterreal (2004) has designed and built a hybrid heat flux measurement system mounted on top of the SSPS-CRS tower at the

Plataforma Solar de Almerı´a (PSA) to measure the incident solar power that is concentrated by a heliostat field on the flat aperture of a central receiver. This device is composed of two measurement systems, one direct and the other indirect. Each direct system component, and in particular, the heat flux microsensors, which enable these measurements to be made in a few seconds without water-cooling, are described. The indirect system is based on a CCD camera that uses a water-cooled heat flux sensor as a reference for converting gray-scale levels into heat flux values. The main objective is to systematically compare both measurements of the concentrated solar power in order to increase the confidence in its estimation. Figure 2.5 shows the compound of non-cooled white target and non-cooled HFM calorimeters array (J. Ballestrin and R. Monterreal, 2004).

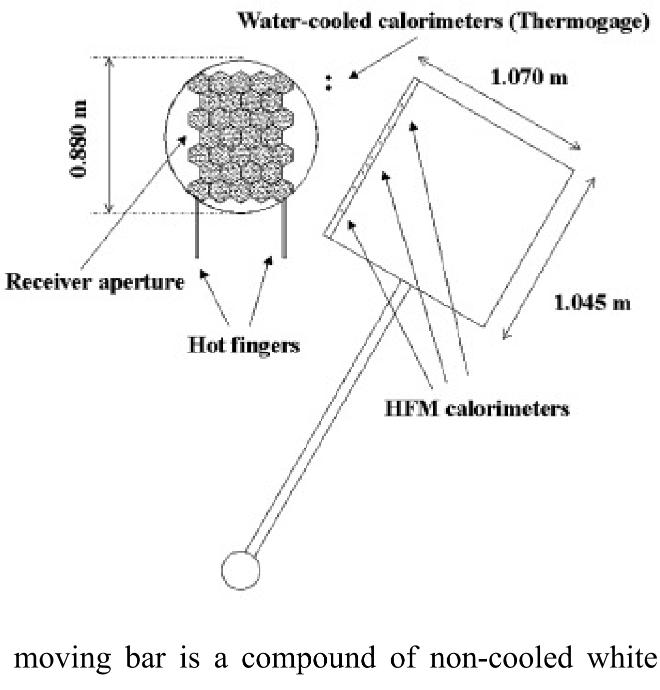

Figure 2.5: The moving bar is a compound of non-cooled white target and non-cooled HFM calorimeters array. The bar passes in front of the receiver aperture obtaining two measurements of the incident power (J. Ballestrin and R. Monterreal, 2004).

The accurate measurement of the concentrated solar flux densities is still a challenge for the research teams working in solar facilities. Calorimeters are accurate instruments, but they cannot keep up with fast variations of the measured flux density, and their range of utilization hardly covers the full range of flux density available in the concentrated solar flux from 50 to 20000 kW/m^2. A Ferriere and B. Rivoire (2002) identified the major parameters of the design of the fluxmeter and proposed an optimized design. They established the expression of the intensity of light reflected by the internal surface of an integrating sphere with an input power provided by a concentrated solar beam. This intensity appears to be proportional to the input power, and thus makes viable the utilization of a photo-sensor interfaced with an integrating sphere to build a solar fluxmeter.

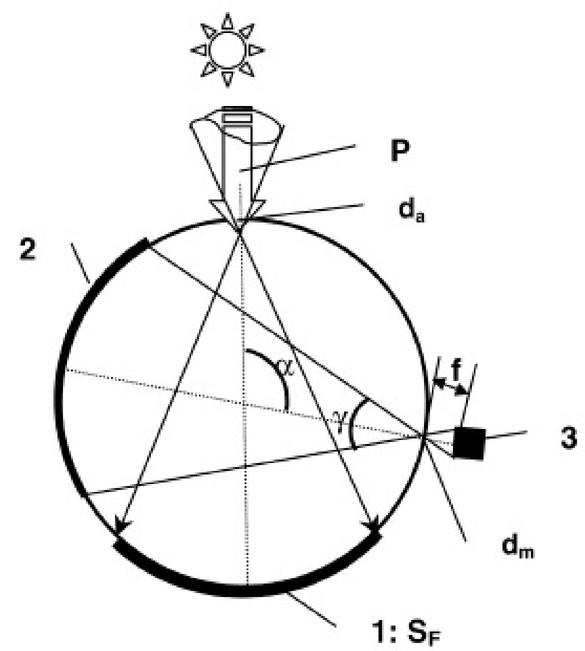

Figure 2.6: Schematic of the fluxmeter using an integrating sphere and a photo-sensor (1) area of first inpact S_F, (2) area of measurement, (3) photo-sensor (A Ferriere and B. Rivoire, 2002).

P. Sansoni *et al.* (2007) developed an experimental procedure for the optical characterization of sunlight collectors, prismatic lenses, optically designed for concentrator photovoltaic cells. The described instrumentation and measurement techniques examine the total collection efficiency of the lens, as well as the energy distribution in the image plane. A specific study has been devoted to investigate the image uniformity, separating the light contributions due to the different lens regions. The image created should be concentrated with the maximum achievable collection efficiency and it should be focused on the squared area of the PV cell with the maximum achievable uniformity.

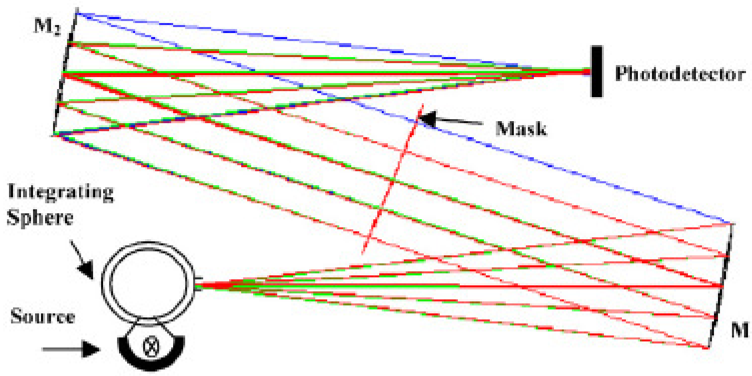

Figure 2.7: Measurement of the light power impinging on the lens (P. Sansoni *et al.,* 2007).

A reliable qualification of solar concentrators is crucial for the prediction of the capabilities of a solar thermal plant. The optical properties of a solar concentrator are strongly dependent on the orientation and mechanical strains that deformed the mirror surface. F. Arqueros *at el.* (2003) presented a novel procedure for the optical characterization of solar concentrators. The method is based on recording at night the light of a star reflected by the mirror. Images of the mirror taken from its focal region allow the reconstruction of the slope map. The application of this technique for the in situ characterization of heliostats is particularly simple at very low cost. Uncertainties in the reconstructed slopes of about 1.0 mrad of Sun have been estimated.

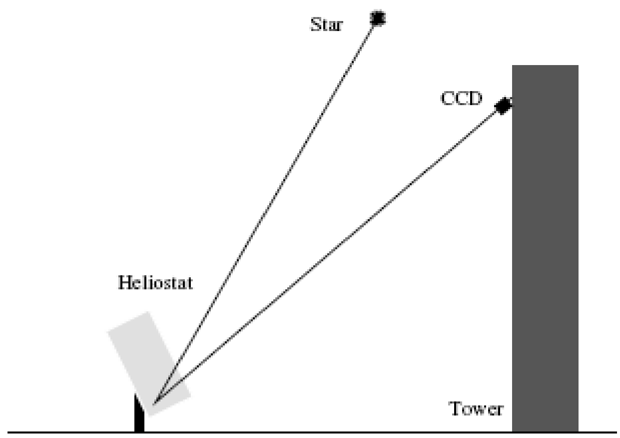

Figure 2.8: Scheme of the SCCAN technique for the optical characterization of heliostats in a central tower system (F. Arqueros *at el.,* 2003).

Digital close range photogrammetry has proven to be a precise and efficient measurement technique for the assessment of shape accuracies of solar concentrators and their components. The combination of high quality mega-pixel digital still cameras, appropriate software, and calibrated reference scales in general is sufficient to provide coordinate measurements with precisions of 1:50000 or better. The extreme flexibility of photogrammetry to provide high accuracy 3D coordinate measurement over almost any scale makes it particularly appropriate for the analysis of solar concentrator systems. Klaus Pottler *at el.* (2005) presented a selection of measurements done on whole solar concentrators and their components. The paper gave an overview of quality indicators for photogrammetric networks, which have to be considered during the data evaluation.

A. Parretta e*t al.* (2007) developed a radiometric method suitable for both total power and flux density profile measurement of concentrated solar radiation. The high-flux density radiation is collected by a first optical cavity, integrated, and driven to a second optical cavity, where it is measured by a conventional radiometer operating under a stationary irradiation regime. The attenuation factor is regulated by properly selecting the aperture areas in the two cavities. The radiometer has been calibrated by a pulsed solar simulator at concentration levels of hundreds of suns.

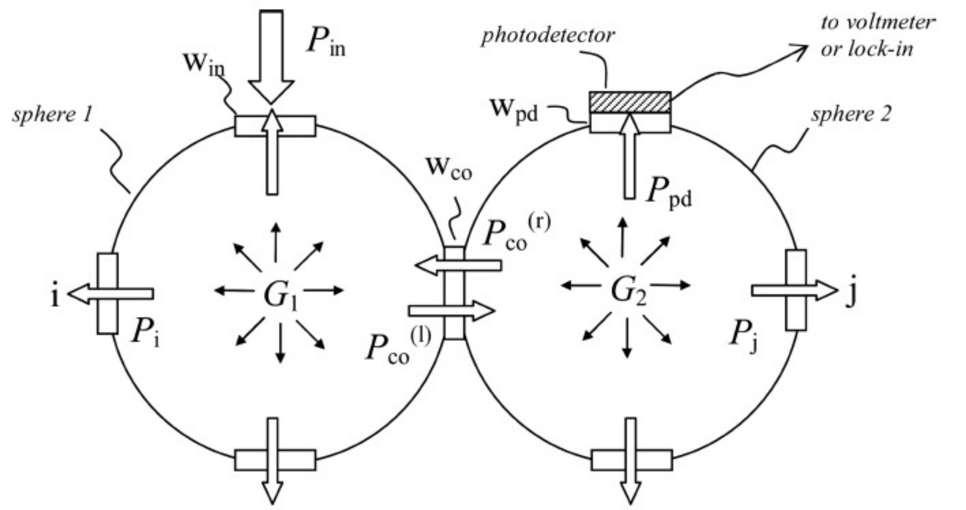

Figure 2.9: General model of the radiometer with two coupled integrating spheres. G_1 irradiance in the first sphere; G_2 irradiance in the second sphere; (w_{pd}) photodetector window for irradiance measurements (A. Parretta e*t al.,* 2007).

Concentrated solar radiation can give temperature above 3000 K. It is fundamentally importance to measure the temperature of the irradiated target. Osamu Kamada (1964) developed a pyrometric method of measuring the surface temperature of a target in a solar furnace by using 1.38-μ wavelength radiation. The measured temperature distribution of irradiated graphite together with the theoretical consideration of the performance is presented. Figure 2.10 shows the arrangement of a solar furnace and an apparatus measuring target temperature while Figure 2.11 shows optical system of the brightness pyrometer.

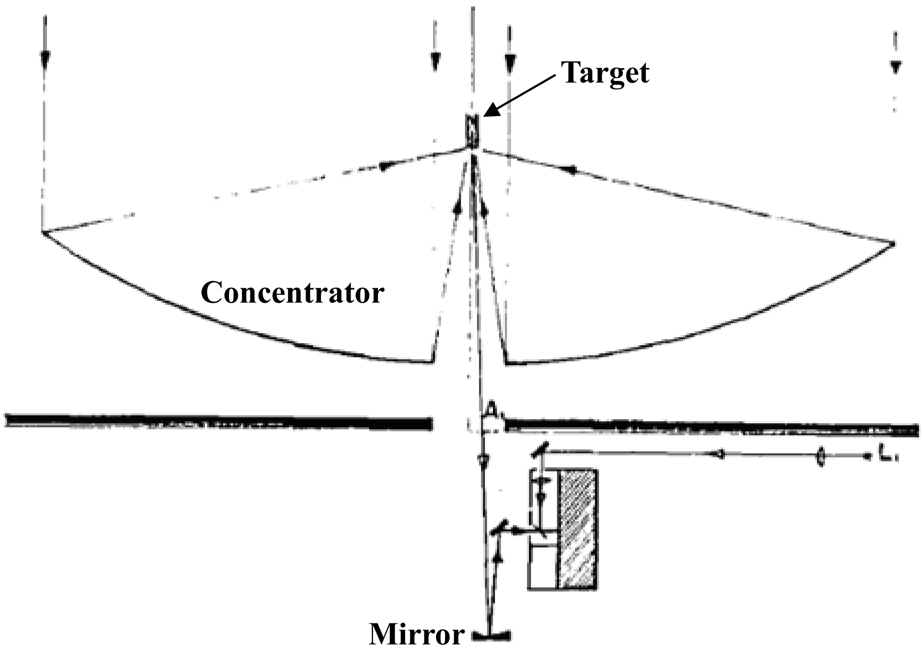

Figure 2.10: Arrangement of a solar furnace and an apparatus measuring target temperature (Osamu Kamada, 1964).

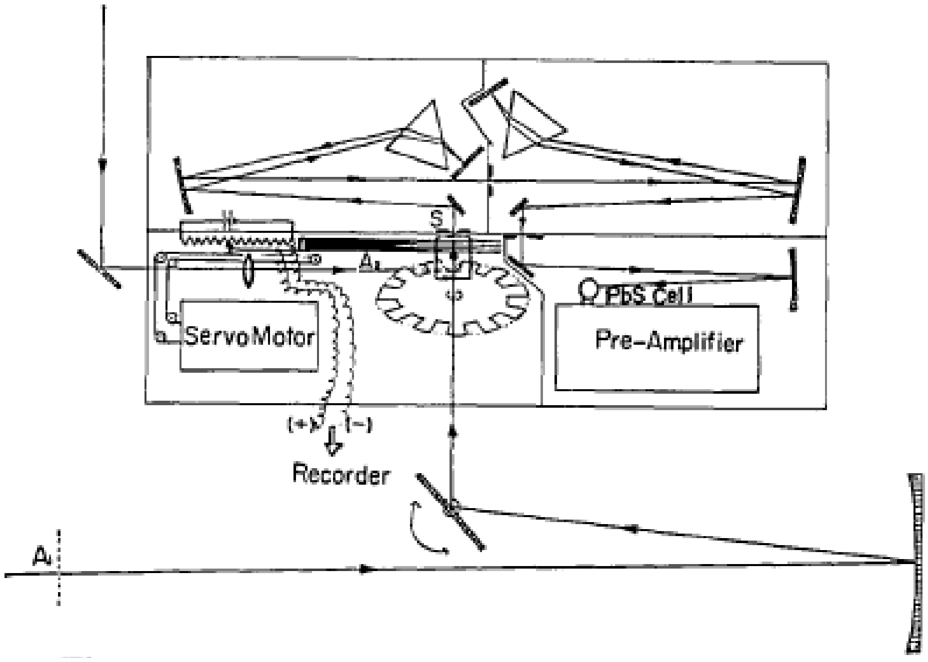

Figure 2.11: Optical system of the brightness pyrometer (Osamu Kamada, 1964).

C.A. Estrada e*t al.* (2007) developed a calorimeter for measuring the concentrated solar power produced by a point focus solar concentrator. The temperature distribution inside the receiving plate of a calorimeter, under concentrated solar irradiation conditions, was determined experimentally. Temperatures are measured at different points of the plate and fit with a theoretical model that considers heat conduction with convective and radiative boundary conditions.

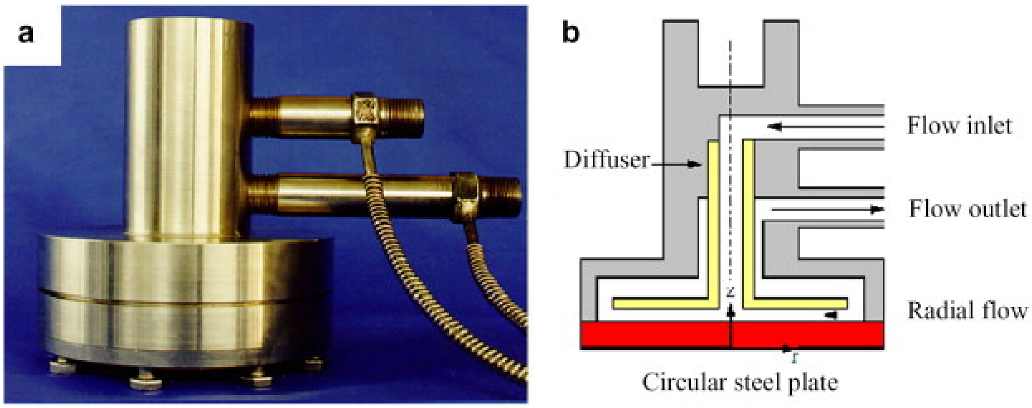

Figure 2.12: (a) Flat plate calorimeter and (b) cross-sectional diagram showing the coordinate axes used in the theoretical model (C.A. Estrada e*t al.,* 2007).

K.-J. Riffelmann e*t al.* (2007) had developed and tested a new flux mapping system to measure flux densities near the focal line of parabolic trough collector, named PARASCAN. With PARASCAN the concentrated sunlight is detected by photodiodes which are placed behind transulucent targets with Lambertian transmission properties. Photodiodes are arranged in two lines: one line is located in front of the receiver (between parabolic mirror and receiver), detecting all incoming sun rays, the other line is placed behind the receiver and registers all rays missing the absorber tube. Figure 2.13 shows the PARASCAN flux scanner mounted on the EuroTrough prototype collector.

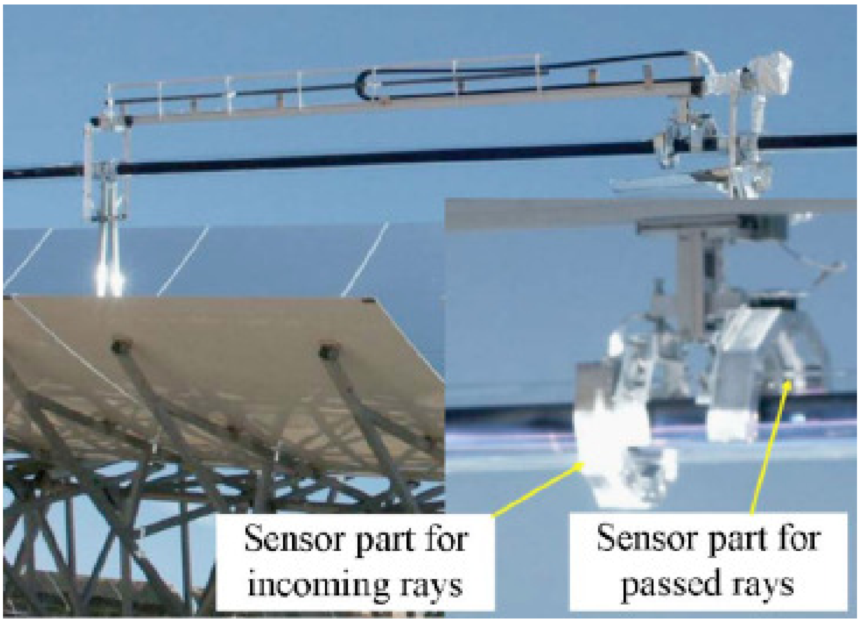

Figure 2.13: PARASCAN flux scanner mounted on the EuroTrough prototype collector, and the two sensor parts (below right, zoomed in) (K.-J. Riffelmann e*t al.,* 2007).

M. Adsten (2004) developed a method to measure the radiation distribution on the absorber of an asymmetric CPC collector with a flat bi-facial absorber. A monitoring device as shown in Figure 2.14 consisting of a photo diode that can slide along the absorber width has been discussed. The photo diode was attached to a device sliding on a potentiometer, allowing both the irradiation and position of the diode to be registered.

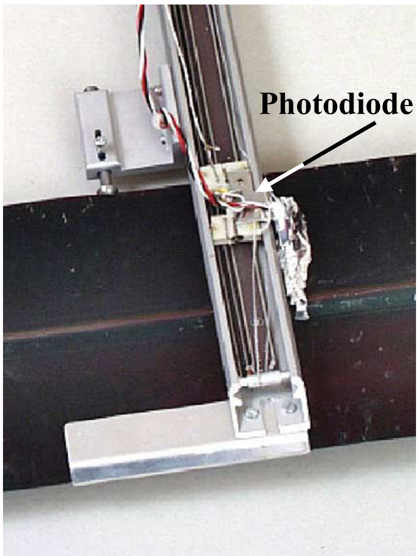

Figure 2.14: Photo of monitoring device attached to absorber. The photodiode is situated at the end of the sliding device (M. Adsten, 2004).

2.2 Simulation Method

K.K. Chong e*t al.* (2010) have carried out a comprehensive analysis vial numerical simulation based on all the important design parameters, i.e., array of facet mirrors, f/D ratio, receiver size, and the effect of sun-tracking error, which lead to the overall optical performance of new concentrator.

The Monte Carlo ray tracing method is the simulation technique widely used in predicting the light flux distribution of various types of solar collector and solar simulator. The Monte Carlo method is a statistical simulation of radiative transfer performed by tracing a finite number of energy bundles through their transport histories. The histories of these energy bundles are traced from their points of emission to their points of absorption. What happens to each of these bundles depends on the emissive, reflective, and absorptive behaviors within the surface; it is described by a set of statistical relationships.

Yong Shuai e*t al.* (2008) used Monte Carlo method to predict radiation characteristics of the solar collector system. The Monte Carlo algorithm is developed to simulate radiation characteristics in the solar collector system and the corresponding model is validated with analytical calculation, COMPREC code, and geometry analytical method. Two important factors (sun shape and surface roughness) that influence the flux profile at the focal plane are studied.

J. Facao and A.C. Oliveira (2011) had carried out a numerical simulation using simplified ray-tracing and computational fluid dynamics (CFD) of a trapezoidal cavity receiver for a linear Fresnel solar collector concentrator. The CFD simulation makes possible to optimize cavity depth and rock wool insulation thickness of the concentrator.

L. Pancotti (2007) developed optimized reverse ray tracing model for flat mirror concentrators that allows reducing the noise and the computing time necessary for the simulations to obtain the irradiance distribution on the absorber of solar concentrator.

R. Leutz, H. P. Annen (2007) have introduced a model using reverse ray-tracing for the evaluation of the performance of stationary and quasi-stationary solar concentrators. Using a simple solar irradiation model, the tilt angle of a novel micro-structured linear concentrator is optimized. They evaluate the yearly energy collection efficiency of the concentrator, using a solar radiation model, and reverse ray-tracing, which depends on latitude and the fraction of direct solar radiation. In reverse ray-tracing, rays originating at the receiver of the concentrator are traced towards the surrounding hemisphere. The method allows for the evaluation of the absolute energy collection: new concentrators may be optimized for location and tilt, requiring one-time ray-tracing. The tilt of existing concentrators is optimized. Only possible solar incidence is considered by their model. The method is fast and realistic; it can be modified for concentrators in tilt operation. Ray-tracing is a statistical method tracing rays of light from a source to a target, e.g. from the sun to a solar concentrator. Ray-tracing can be time-consuming, since for an error of $\sqrt{n}/n$, n rays have to be traced for any bin, where a bin is a combination of parameters like solar azimuth and elevation, or location on the receiver. Reverse (or backward) ray-tracing in combination with a solar radiation model can simplify this procedure by tracing only rays that are of interest, omitting those that come from impossible positions of the sun. Source becomes target, and vice versa; now the receiver of the concentrator illuminates part of the hemisphere above. The concentrator optics modify the rays' paths. Backward ray-tracing has been used in the past in order to evaluate flux distributions on cylindrical solar concentrators, where a grid of rays was traced from the receiver towards the sun. The flux of each ray was calculated according to the location, where it hit the solar disk, using a model of the solar brightness distribution.

CHAPTER 3

METHODOLOGY

3.1 The Optical Scanner

A novel optical scanner with the resolution of about 1 cm^2, equal to the photo-sensitive area of a single unit photodiode used in the scanner, and capable of performing one complete measurement cycle within a time period of 5 seconds had been designed, constructed, and tested in Universiti Tunku Abdul Rahman (Chong and Yew, 2011).

The high speed scanning method of the optical scanner can allow us to map a reasonably high resolution light flux distribution pattern with a total coverage area of 1125 cm^2, where the light flux is defined as the photon energy per square-meter per second with the unit of W/m^2.

For a complete measurement, 1125 readings are taken by the photodiodes array for a plane with total surface area of 45 cm × 25 cm. The rapid measurement enables us to analyze the collected data almost instantaneously by plotting a flux distribution map after all the data is transferred to the computer.

Figure 3.1 shows the major components of the optical scanner. The optical scanner consists of an array of photodiodes, amplifier circuit, microcontroller, stepper motor, multiplexer circuit and computer. The light flux measurement and data acquisition of the optical scanner are controlled by a computer with a custom designed user interface program.

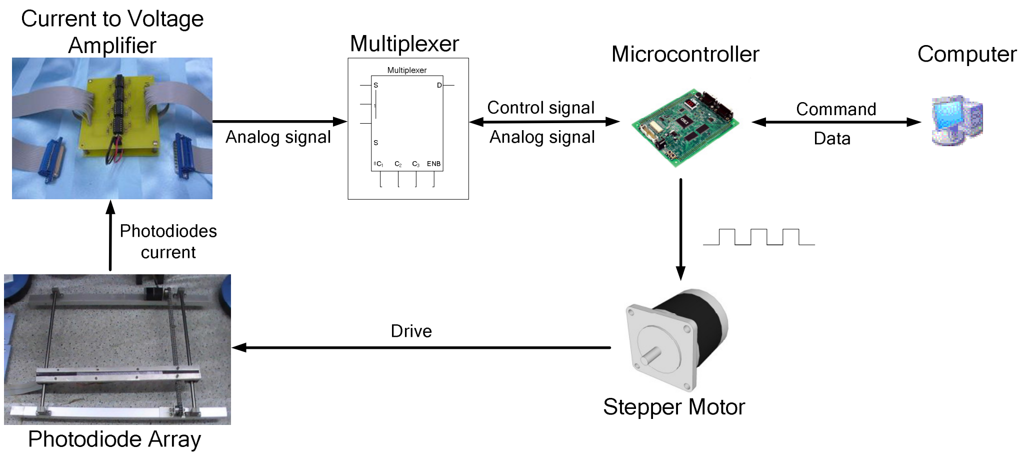

Figure 3.1: Schematic diagram to show the major components of the novel optical scanner.

3.1.1 Photodiode

The photodiodes used in the optical scanner are solderable planar photodiodes with photo-sensitive area of 1 cm^2. The planar photodiode was chosen as it can be fixed on an aluminum heat sink using thermal adhesive for cooling purpose. The selected photodiodes are able to respond linearly to the irradiance of the detected light over the range of 0 – 1000 W/m^2. Figure 3.2 shows the diagram of solderable planar photodiode with its dimension. The photo-sensitive area of the photodiode will determine the resolution of the optical scanner which is 1 cm^2. The photodiodes have a protective coating that protects them from humidity effects and also provide a reliable and inexpensive detector for instrumentation and light beam sensing applications.

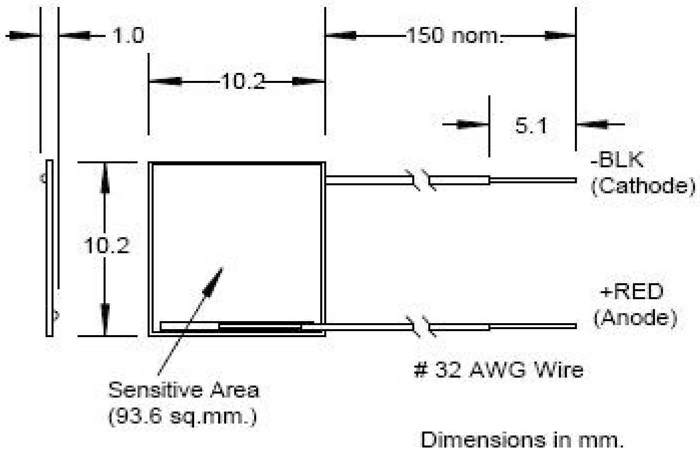

Figure 3.2: Diagram of solderable planar photodiode with its dimension.

3.1.2 Stepper Motor and Microstep Driver

Figure 3.3 shows the DC geared type stepper motor with gear ratio 1:7.2 that used in the optical scanner is able to perform very accurate positioning with the rotation of very fine step of 0.25°. Figure 3.4 shows the microstep driver that used to drive the stepper motor.

The specifications of the stepper motor are list as below:

Maximum holding torque: 0.3 N m

Basic step angle: 0.25°

Permissible speed range: 0~250 r/min

Figure 3.3: Geared type stepper motor used in the optical scanner with gear ratio of 1:7.2.

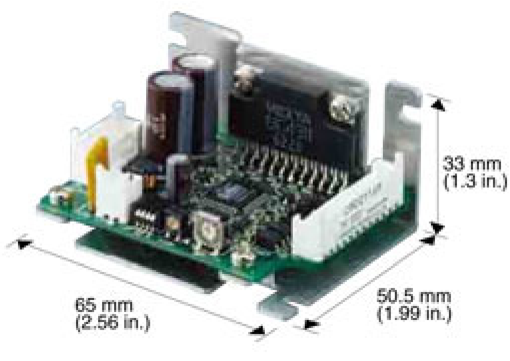

Figure 3.4: Mircrostep driver of stepper motor.

3.1.3 Microcontroller

Figure 3.5 shows pin diagram of PIC18F4550 microcontroller used to generate motor stepping pulses and data acquisition.

40-Pin PDIP

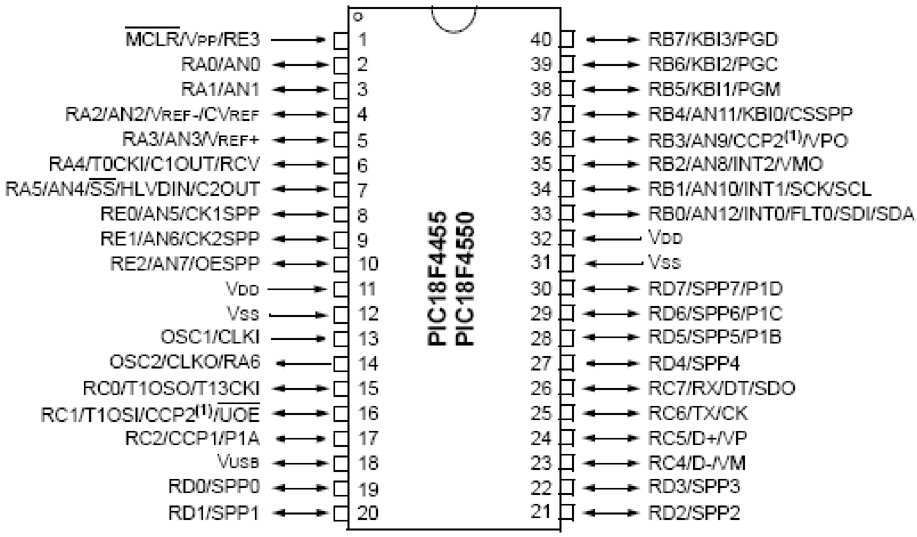

Figure 3.5: Pin diagram of microcontroller PIC18F4550.

Two important features of PIC18F4550 were utilized in the optical scanner operation:

1. UNIVERSAL SERIAL BUS (USB) V2.0 Compliant: PIC18F4550 incorporate a fully featured Universal Serial Bus communications module that is compliant with the USB Specification Revision 2.0. The module supports both low-speed and full-speed communication for all supported data transfer types. It also incorporates its own on-chip transceiver and

3.3V regulator and supports the use of external transceivers and voltage regulators.

2. 10-bit, up to 13-channel Analog-to-Digital Converter module (A/D) with Programmable Acquisition Time: This module incorporates programmable acquisition time, allowing for a channel to be selected and a conversion to be initiated, without waiting for a sampling period and thus, reducing code overhead.

3.1.4 Multiplexer

The multiplexer used is HCF4053B, which is a triple 2-channel analog multiplexer. The propagation delay of the signal from input to output is very short, i.e:30 ns. The fast switching speed enables the data acquisition in high speed. Figure 3.6 shows the pin diagram of HCF4053B multiplexer.

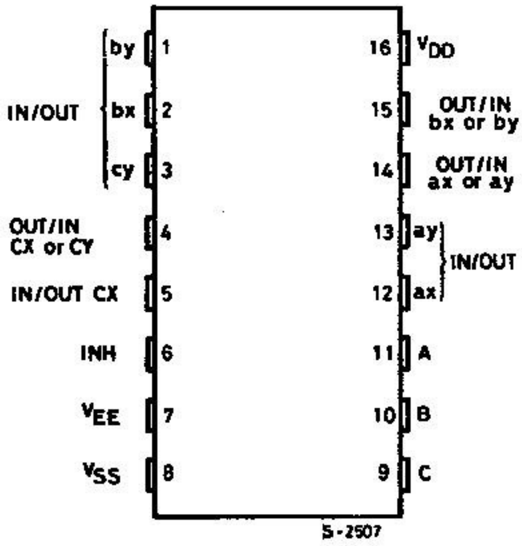

Figure 3.6: HCF4053B triple 2-channel analog multiplexer.

3.1.5 Operational Amplifier

TL084A is the general purpose J-FET quad operational amplifiers use to convert and amplify the photodiode output current to voltage that read by ADC. Figure 3.7 shows the pin diagram of TL084A op-amp. The op-amp has very low input offset current which will greatly reduce noise and error of output signal after the amplification.

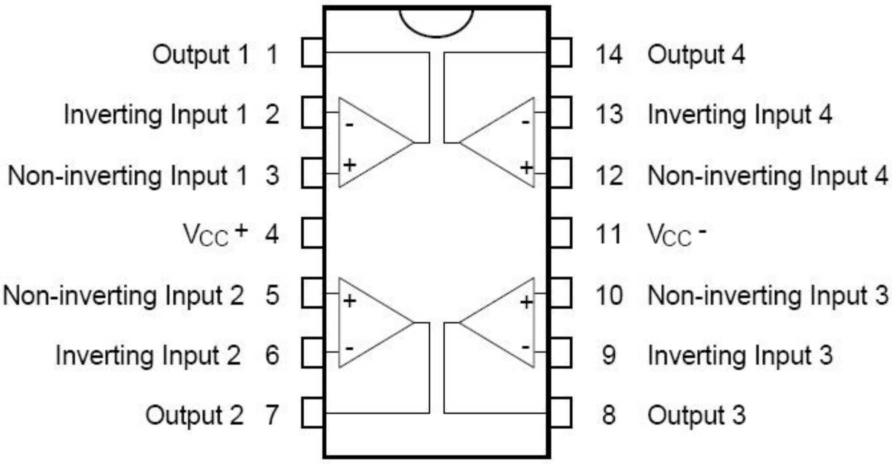

Figure 3.7: Pin diagram of general purpose J-FET quad operational amplifiers TL084A.

3.1.6 User Interface Program

A user interface program was developed to control the whole measurement process. It is capable of sending commands to the microcontroller to perform desired functions such as to collect and to process the measurement results. The user interface shown in Figure 3.8 was developed using Delphi programming language.

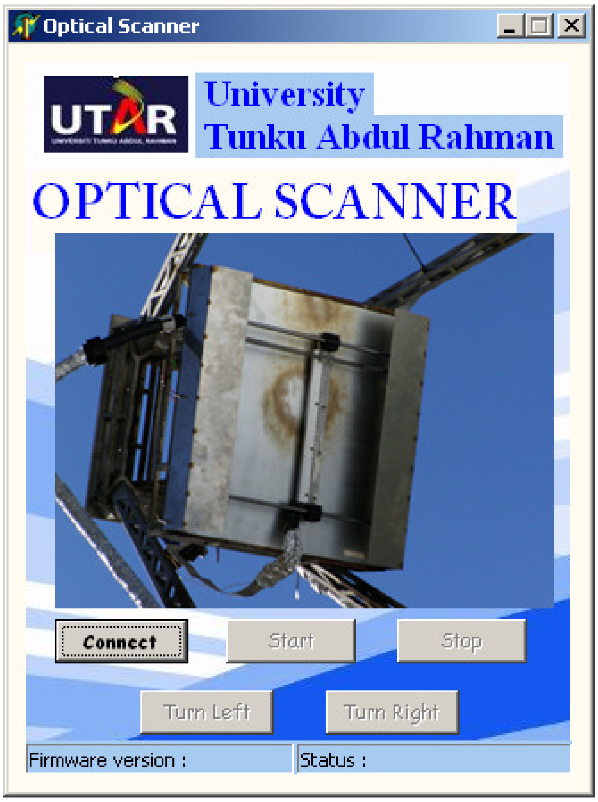

Figure 3.8: Graphic user interface of optical scanner

3.2 Optical Scanner Design

In the design of the novel optical scanner, planar photodiodes were employed to detect the incoming light irradiance. The photodiodes are relatively small in size with a photo-sensitive area of 1 cm^2, constituting the basic pixel of the light flux distribution map.

A single row of n photodiodes is used in the novel optical scanner to measure the light irradiance across a squared or rectangular plane. This method can greatly reduce the number of sensors used and the cost of the device as compare to the $m \times n$ photo-sensors method.

In this optical scanner, 25 planar photodiodes are arranged in a single row and attached to an aluminum holder to form a photodiode array. The photodiodes are arranged closely to adjacent photodiodes to avoid blank gaps that will affect the resolution of the flux distribution maps. The arrangements of the photodiodes are shown in Figure 3.9. All the photodiodes are slotted into a slot on the thin aluminum bar and the aluminum surface beneath the photodiodes is insulated from the photodiode itself with thermal adhesive material that is thermally conductive but electrically insulated to avoid short circuiting because the output current from each photodiode had to be read separately to determine the light irradiance level at that particular pixel.

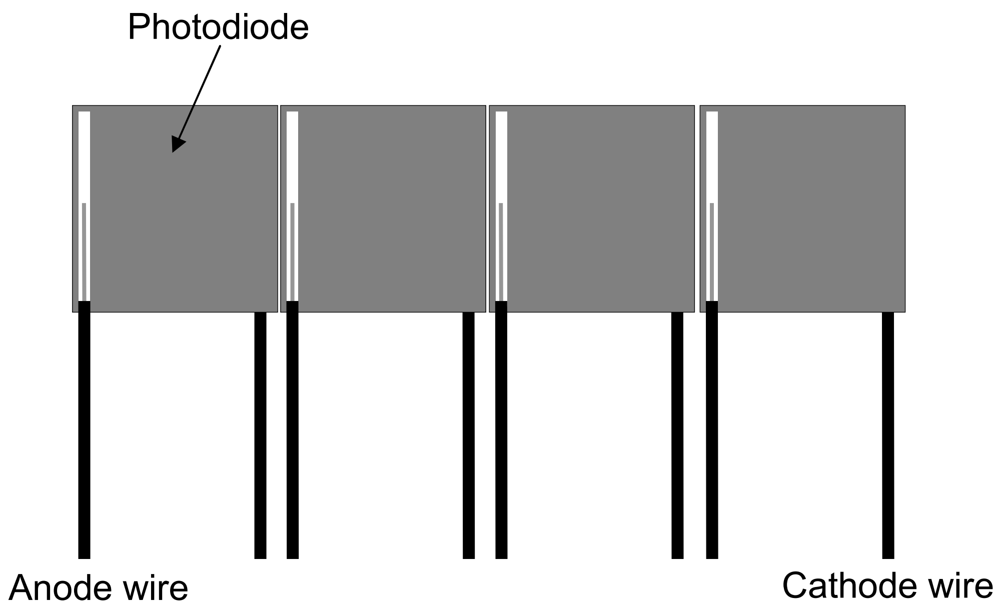

Figure 3.9: The arrangements of 4 of the photodiodes in the photodiodes array.

On the top surface of the photodiode array, a stainless steel cover that contains 25 equally distant circular apertures with a diameter of 2.5 mm each is placed in such a way that each aperture is located over the center of each photodiode. The apertures located 3 mm above the photodiodes were used to block part of the diffuse component of the light so that the photodiode mainly detects the directional or beam component of the light that enters the aperture. The cover also serves as light attenuator to prevent heat from the light source to heat up the photodiodes. The small aperture can decrease the output current as well as the heat generated from the photodiode in order to simplify the electronic circuit design. Temperature variation will change the responsivity of photodiode (Parr *et al.*, 2005), therefore this approach is to maintain the same operating temperature of the photodiodes throughout the measurement to keep the responsivity change of photodiodes negligibly small.

For the choice of aperture, there is a relationship of both the aperture distance from the photodiode and the size of aperture with the field of view of the photodiode as illustrated in Figure 3.10. The priority for the design of the aperture was to aim at reducing the heat absorbed by the photodiode and thus to reduce the signal noise that can be caused by the temperature variation. Therefore, the field of view of the current design was 102.68°, which is less than the 160° standard required for a solar simulator. However, the current optical scanner can be easily modified to comply with the standard required for a solar simulator by reducing the distance between the aperture and the photodiode, *h*, to 0.32 mm.

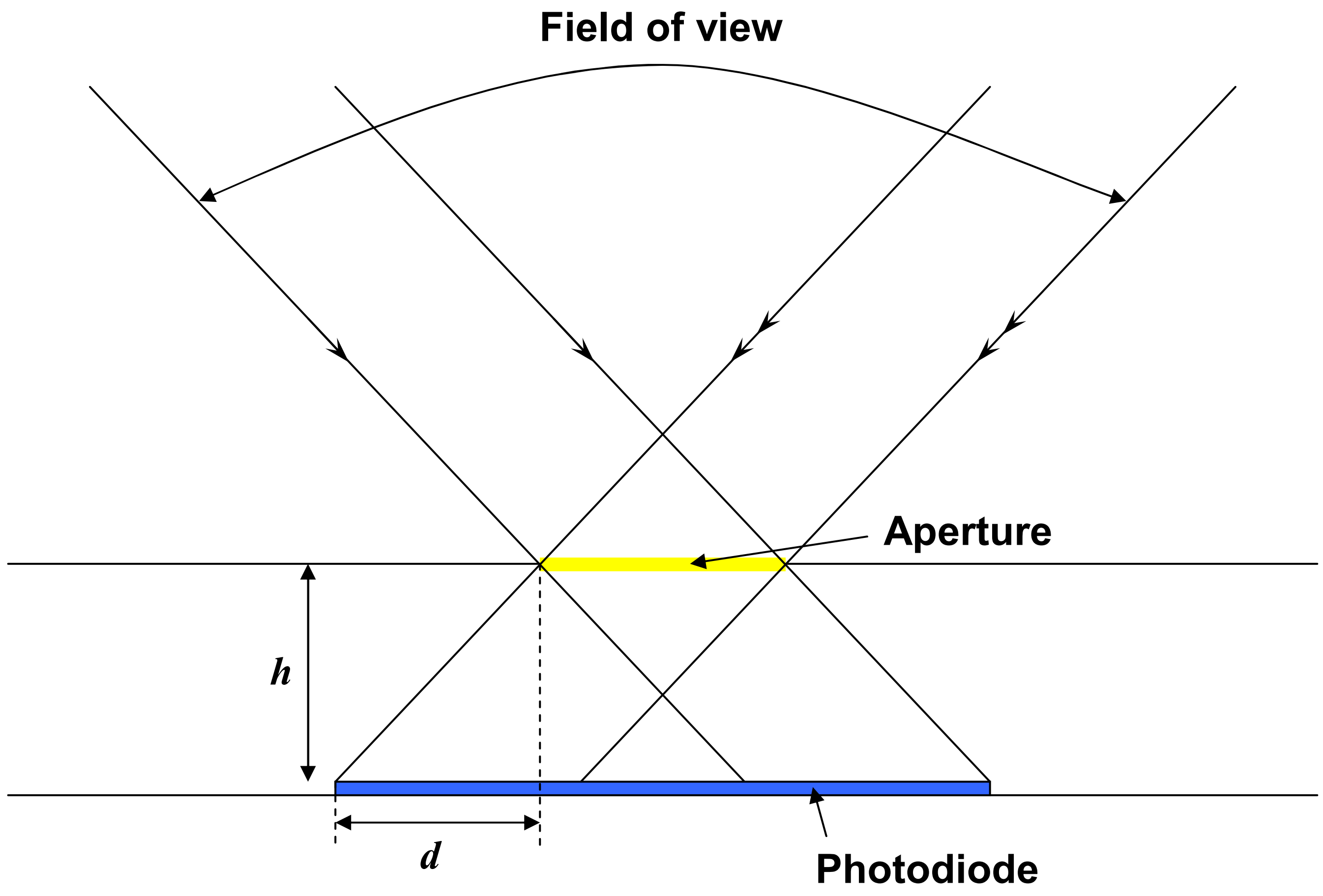

Figure 3.10: Schematic diagram to show the calculation of field of view of the photodiode.

The calculation of the angular field of view is demonstrated as follow: Field of View is defined as FOV = 180° – 2 $\tan^{-1}$ (h/d), where d is the half width of photodiode minus the radius of aperture and h is the distance between aperture and photodiode.

Based on the current design, FOV = 180° – 2 $\tan^{-1}$ (3 mm / 3.75 mm) = 102.68°.

The photodiode aluminum holder was mounted on a linear slider and driven by a stepper motor via a metal chain. The shaft of the stepper motor can rotate in steps according to the step pulses generated by the microcontroller. The microcontroller generates 3000 pulses per second to drive the photodiode array at a speed of 9 cm per second. The positioning of the photodiode holder has proven to be robust, consistent and highly accurate with negligible backslash even after many measurement runs had been performed.

The high speed scanning can also overcome the problem of heat management of the photodiode array due to the short exposure time to the light irradiance. In the optical scanner design, the initial and final positions of photodiode array are set to be off from the illuminated area of light source so that the photodiodes are not heated up and the effect of the temperature to the measurement result can be minimized. In this case, passive cooling is sufficient by using an aluminum heat-sink connected to the rear side of the photodiode array.

Figure 3.11 shows the optical scanner with a single row of photodiodes that scans in a direction from top to bottom. All the photodiodes are covered by a stainless steel plate with small apertures to expose the surface of the photodiodes. The square cells as shown in Figure 3.11 denote the positions at which the readings of light irradiance is acquired and subsequently sent to the microcontroller. During the process of data acquisition, the readings are collected simultaneously for all the photodiodes arranged in the same row and then the scanner is shifted to the next row after the readings are stored. The position and the reading of each cell are recorded by the microcontroller and these data are sent to the computer for further processing and analysis.

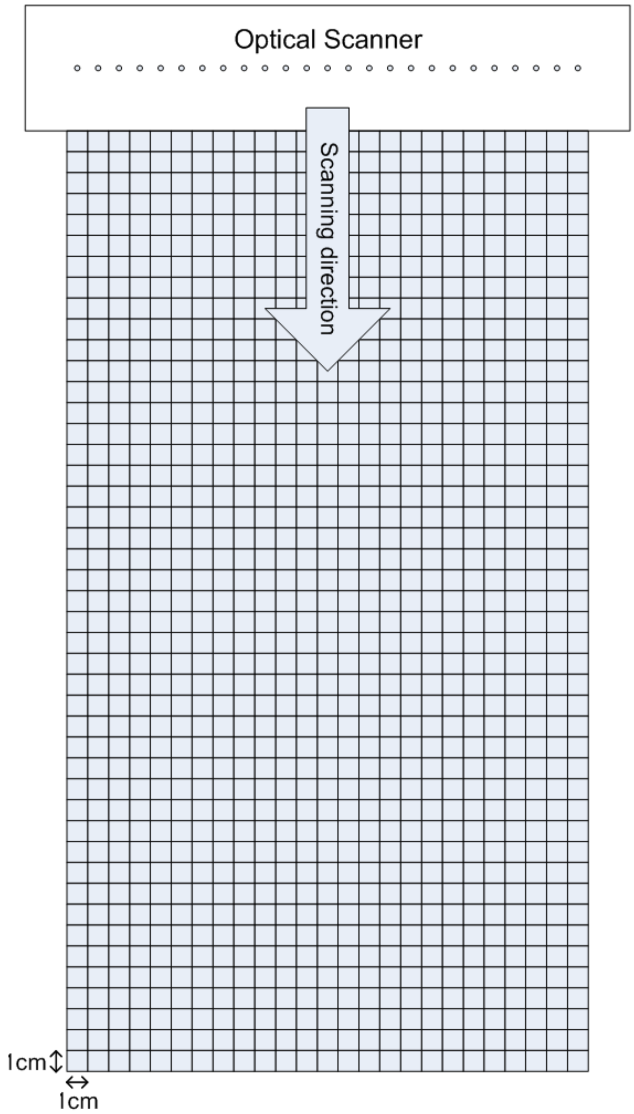

Figure 3.11: Small cell representing the position and the area of each measurement during the scanning process. The square cells as shown in the above schematic diagram denote the positions at which the readings of light irradiance are acquired and subsequently sent to the microcontroller. During the process of data acquisition, the readings are collected simultaneously for all the photodiodes arranged in the same row and then the scanner is shifted to the next row after the readings are stored.

Each individual photodiode was calibrated to obtain the relationship between the light irradiance and photodiode output current. All the photodiodes were calibrated against a standard radiometer, EPPLEY pyrheliometer Model NIP, which provides absolute irradiance level of the light irradiance. Figure 3.12 shows the pyrheliometer used for the measurement of normal incident solar irradiance.

Figure 3.12: Pryheliometer that measure normal incident sunlight. (US Resource Assessment, 2011).

Using the calibration information, measurements can be correlated with the absolute value of irradiance level. Figure 3.13 shows the calibration graph for one of the photodiodes used in the optical scanner. All the calibration graphs show very good linear relationship between the output current of photodiode and light irradiance since the R-squared values of all the linear graphs are higher than 0.95. Regression analysis of the graphs has been carried out to study the standard error of the regression lines. The standard errors of all regression lines have been calculated and were within the range of 2.61% to 3.67% when they were compared using the error of the mean of the dependent variable. The standard errors appear to be small and hence the linear regression model of light irradiance as function of the photodiode current was determined to be good. The absolute value of the light irradiance detected by the photodiode used in the calibration graph as revealed in Figure 3.13 can be calculated as follow:

$$\text{Light irradiance, } \boldsymbol{I}\ (\text{Wm}^{-2}) = R_e \times I_{ph} \times Gain + \boldsymbol{I}_{offset}$$

where I_{ph} is the photocurrent of photodiode (mA), *Gain* is the amplification gain of photodiode output signal, and R_e is the responsivity per unit area of photodiode, which is a constant to describe the performance of photodiode in terms of the photocurrent generated per incident optical power per unit area ($\text{Wm}^{-2} \cdot \text{mA}^{-1}$) and it can be obtained from the slope of the calibration graph as shown in Figure 3.13. $\boldsymbol{I}_{offset}$ is a constant and it can be obtained from the graph as shown in Figure 3.13 when the photocurrent output, I_{ph}, is zero (mA).

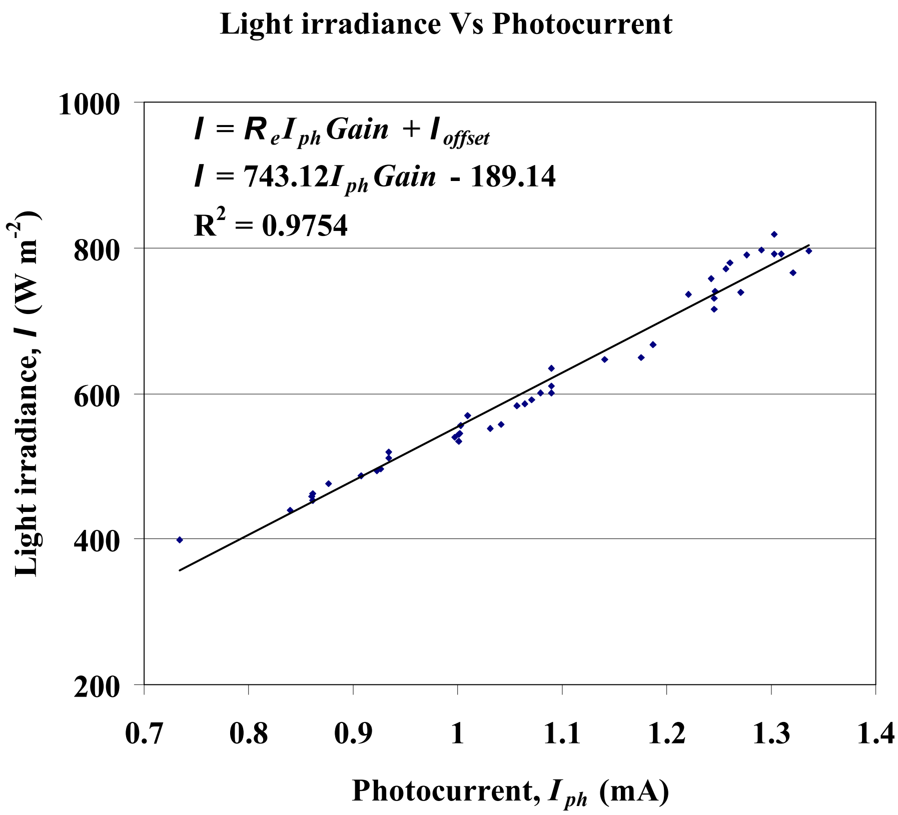

Figure 3.13: Calibration graph for one of the photodiodes installed on the measurement array.

The output signal of the photodiode can be measured as a voltage or a current. Current measurements demonstrate far better linearity, offset, and bandwidth performance. The generated photocurrent is proportional to the incident light power per unit area. Photodiodes and Op-Amps can be coupled such that the photodiode in a short circuit current mode. The op-amp functions as a simple current to voltage converter also known as a trans-impedance configuration amplifier. In the configuration of current-to-voltage converter, the photodiode can be operated with or without an applied reverse bias depending on the specific application requirements. They are referred to as "Photoconductive" (biased) and "Photovoltaic" (unbiased) modes.

In the photovoltaic mode, the photodiode is unbiased; while for the photoconductive mode, and external reverse bias is applied. Mode selection depends upon the speed requirements of the application, and the amount of dark current that is tolerable.

The most precise linear operation is obtained in the photovoltaic mode, while higher switching speed s realizable when the diode is operated in the photoconductive mode, as shown in Figure 3.14, at the expense of linearity. Under these reverse bias conditions, a small amount of current called dark current will flow even when there is no illumination. There is no dark current in the photovoltaic mode. In the photovoltaic mode, the diode noise is basically the thermal noise generated by the shunt resistance. In the photoconductive mode, shot noise due to conduction is an additional source of noise. Photodiodes exhibit their fastest switching speeds when operated in the photoconductive mode.

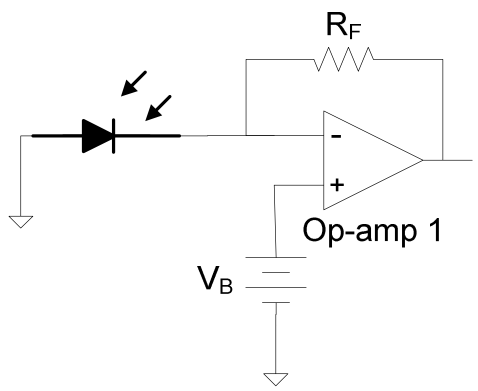

Figure 3.14: Photoconductive mode: reverse bias, has "dark" current, higher noise (Johnson + shot), high speed applications.

When a photodiode is used in the photovoltaic mode, the voltage across the diode is kept at zero volts. Consequently, this almost eliminates the dark current altogether (Wilson, 2005; Jung, 2006). Thus, the shot noise due to the dark current is also negligible and it thus increases the precision of the output signal. In addition to offering a simple operational configuration, the photocurrents in this mode have less variation in responsiveness with temperature. For this purpose, we have configured the current-to-voltage converter in photovoltaic mode as shown in Figure 3.15.

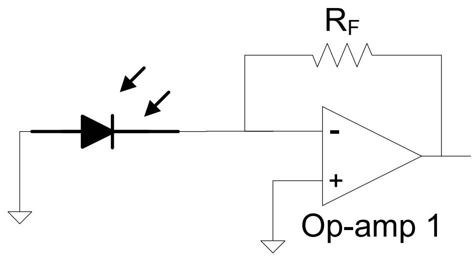

Figure 3.15: Photovoltaic mode: zero bias, no "dark" current, low noise (Johnson), precision applications.

Although the shot noise is negligible in the photovoltaic mode, other noises found in the electronics circuit still exist including thermal noise of the photodiode, thermal noise of the feedback resistor in the amplifier, and the input offset current of the amplifier. The thermal noise of the feedback resistor and the thermal noise of the photodiode are expressed in the equations $I_N = [4kT/R_F]^{½}$ and $I_{TH} = [4kT\Delta f/R_{SH}]^{½}$, respectively, where k is the Boltzmann's constant, T is the absolute temperature of the photodiode, R_F is the feedback resistance of the amplifier circuit, R_{SH} is the shunt resistance of the photodiode, and Δf is the bandwidth of the photodiode. The total calculated noise was 8.66×10^{-7} A and the equivalent noise output voltage was 0.234 mV when it was amplified by a gain of 270. Hence, the error signal caused by the various noises was relatively small and negligible.

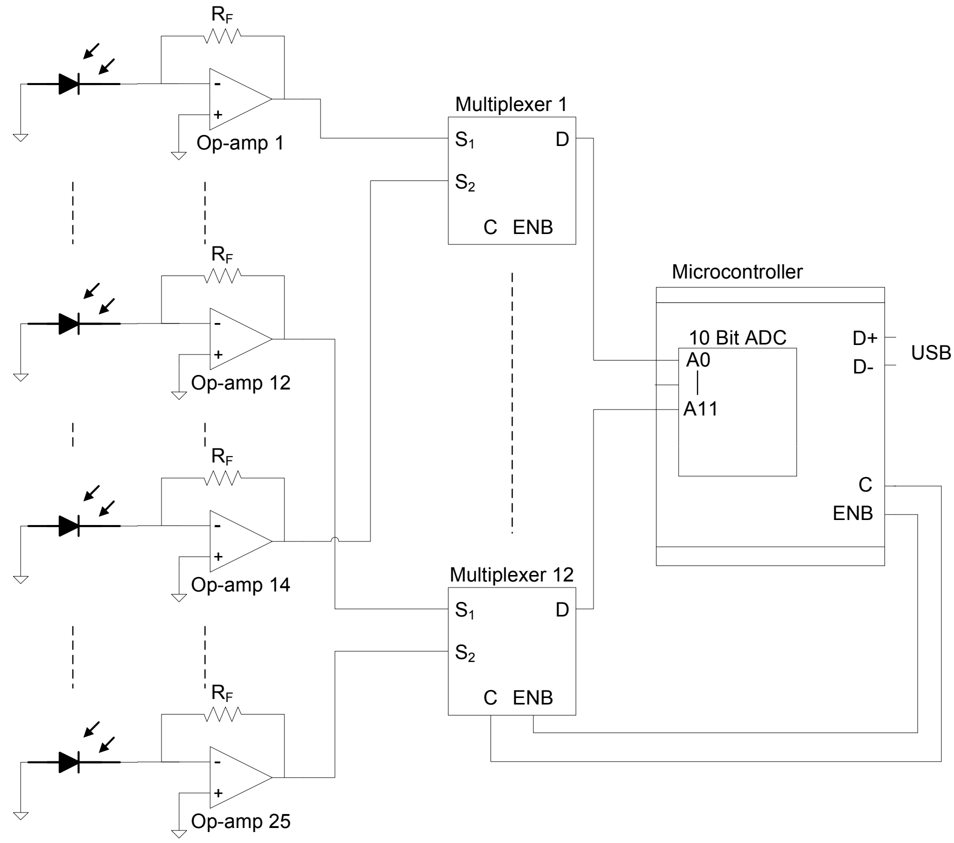

Figure 3.16: The overall architecture of the photodiodes and the accompanying electronic circuit.

After converting the signals from current to voltage, the voltage signals were amplified and read by a microcontroller through a multiplexing circuit. The analog data were converted to digital data first via 10 bits Analog-to-Digital Converter (ADC) and the digital signals were then transferred to the computer. In the conversion, a Least Significant Bit (LSB) represented an equivalent value of 4.88 mV, with a reference of 5 V as maximum voltage. When the equivalent value was translated into light irradiance using the calibration graph, the equivalent light irradiance value was 3.6 W/m^2. ADC conversion contains errors that are integral linearity errors, differential linearity errors, offset errors, and gain errors. The total error was 4.5 LSB or equivalent to 16 W/m^2. The accuracy of the system is basically limited by the ADC error, so the resulting light irradiance had accuracy in the range of $\pm$ 16 W/m^2.

The total response time of the electronic circuit and photodiode was determined by the rise time of the photodiode, slew rate of the trans-impedance amplifier, multiplexer propagation delay time, and the acquisition and conversion time of the ADC. The photodiode had a rise time of less than 4 μs. The amplifier had a slew rate of 8 V/μs of which it took 0.625 μs to increase from 0 V to 5 V, representing the maximum voltage read by the optical scanner. The delay time of the multiplexer was 360 ns, and the total response time of ADC was 4.2 μs. The total maximum time to read a signal from a photodiode until the signal could be converted to a digital signal and then stored in the register was approximately 9.185 μs. Hence, it took a maximum time of 229.625 μs to complete the data acquisition process by the photodiodes array. The response time of the data acquisition system is fast enough compared to the time it took to shift the photodiode holder by 1 cm, which was approximately 111 ms.

3.3 Operating Procedure

Figure 3.17 shows the operational flow chart of the optical scanner, respectively. The optical scanner is placed in the measurement plane in which the sensors surface is normal to the light beam. The process is started by sending a command from the computer to the microcontroller through USB communication. The microcontroller will check the USB communication status before starting to perform measurements. After the USB connection is established, the aluminum holder will be shifted 1 cm by the stepper motor. To shift the aluminum holder, the microcontroller has to calculate the number of steps needed to run the stepper motor for 1 cm of movement. After the calculation, microcontroller will generate the required number of step pulses and the pulses will trigger the stepper motor driver to drive the stepper motor.

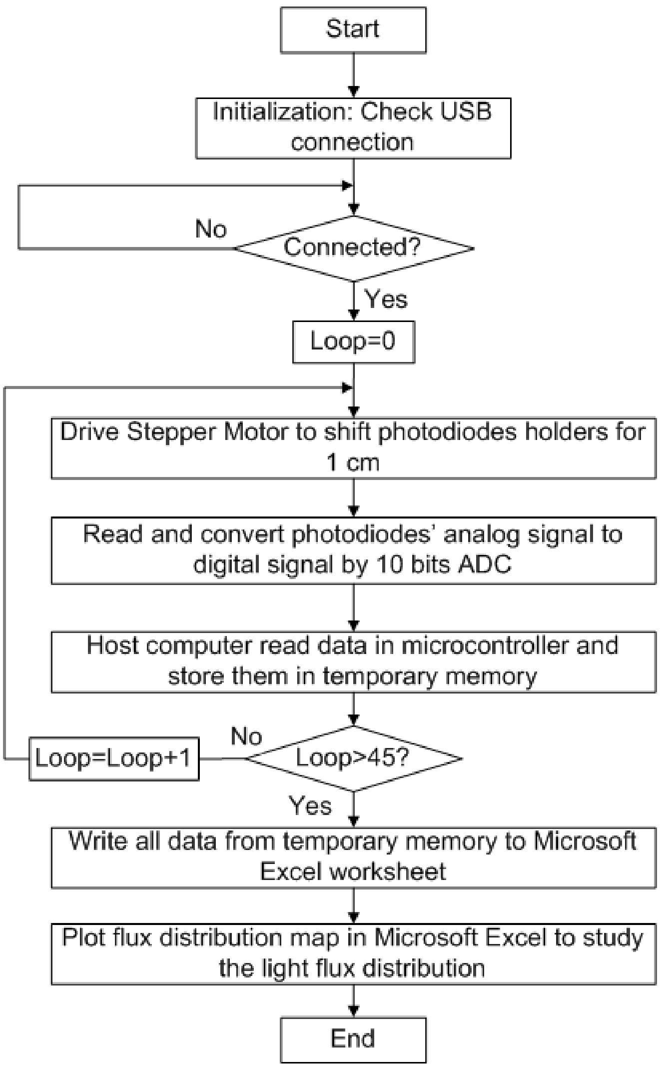

Figure 3.17: Flow chart of the optical scanner operation.

For each centimeter of the photodiodes array shifted, the microcontroller will read the output signal from each photodiode through a high speed multiplexer circuit. The analog data is then converted to 10 bits binary numbers by an ADC and the digital data is stored in the USB communication registers of the microcontroller. After the conversion process is completed, the registers are read by the host computer. The computer will then store the data in a temporary memory array. This data collection process is repeated for 45 times, equaling the 45 cm in total distance the sensors holder has to be moved as shown in Figure 3.11. After the whole process is completed, the data stored in the temporary memory array is converted from voltage value to light irradiance value using the calibration factor obtained from the calibration graph. The irradiance values are written to a Microsoft Office Excel worksheet and the contour map is then plotted.

CHAPTER 4

EXPERIMENT SETUP and RESULTS

4.1 Experiment Setup

4.1.1 Artificial Light Sources

The optical scanner has been tested to measure the light flux distribution maps of two selected artificial light sources. The non-uniform light source is a good reference to test the capability of the optical scanner for detecting the variation of irradiance. The first light source tested was an artificial light source consisting of three motorcycle xenon headlamps of 35 W each. The second light source was also an artificial light source comprised of three commercial xenon lamps of 20 W each. The distance between both artificial light sources and the scanner was fixed at 50 cm. All the lamps used during the measurement were reasonably new with the total operating time of less than 5 hours. Figure 4.1 shows the experiment setup of optical scanner with light source consisting of motorcycle xenon headlamps of 35 W each.

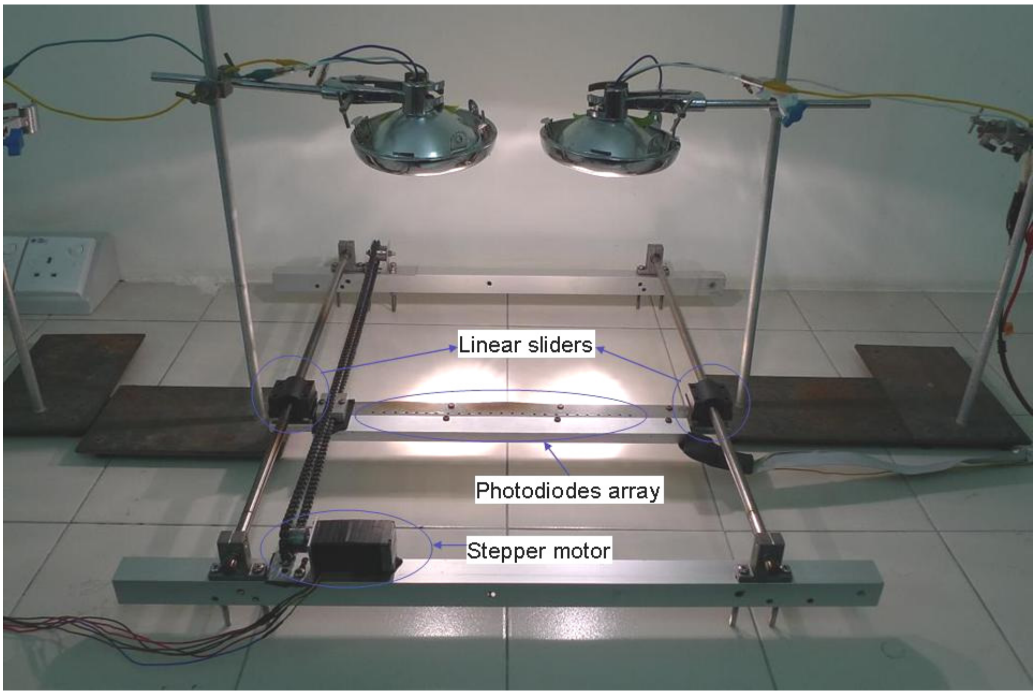

Figure 4.1: Experimental setup of the optical scanner with light source consisting of motorcycle xenon headlamps of 35 Watt each.

4.1.2 Sunlight

The third light source was the sunlight with a direct normal irradiance of 752 W/m^2 as measured by a pyrheliometer. During the measurement, the optical scanner was setup in a way that the incident sunlight is normal to the measurement surface of the scanner. The measurement was made during the noon time under a very clear sky.

4.1.3 Solar Flux Distribution for Different Thickness of Mirror

Figures 4.2 and 4.3 shows the experimental setup of the optical scanner to measure the solar flux distribution for different thickness of mirror. The specimen flat mirror is fixed at the position as near to the centre of the NIPC concentrator as possible to minimize cosine loss with the target distance of 4.5 m from the receiver plane where the optical scanner is located. The optical scanner is placed at the target plane of prototype non-imaging planar concentrator in which the sensors surface is normal to the incident light beam at the target. The solar concentrator was tracking the sun during the measurement was made.

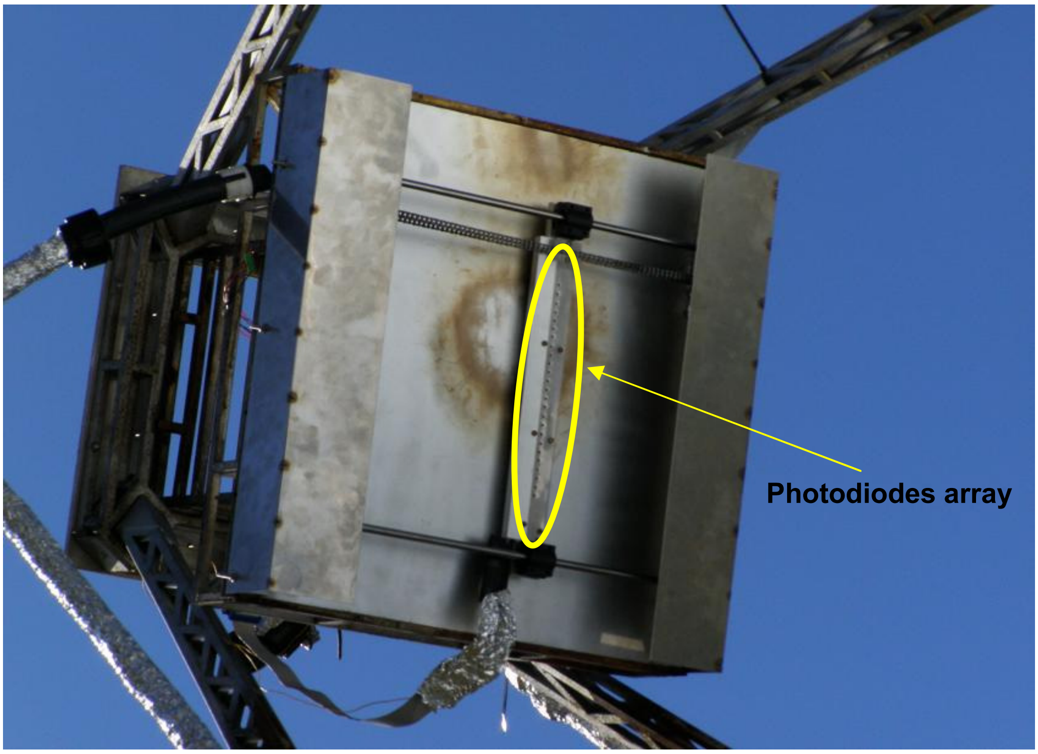

Fig. 4.2: Experiment setup of Optical Scanner

Fig. 4.3: Prototype of Non-Imaging Planar Concentrator (NIPC) with all the mirrors blocked with black plastic cover except the specimen mirror. The specimen flat mirror with different thickness has been tested under the sun.

The measurement results are later compared with the simulation result from the numerical simulation method developed by Chong *et al.* (2010) and it was modified for simulation of image reflected by a single mirror.

4.2 Results

4.2.1 Artificial Light Sources

Figures 4.4(a) and (b) show the light distribution pattern of the first artificial light source from a picture taken by CCD camera and a contour map generated by the optical scanner, respectively. Similarly, Figures 4.5(a) and (b) reveal the light distribution patterns of the second artificial light source from a picture taken by CCD camera and a contour map generated by the optical scanner, respectively. The variation in the irradiance of the two artificial light sources can be easily identified from the contour maps with a resolution of 1 cm^2 within the measurement plane.

The measurement results of the optical scanner were compared with grayscale picture taken by the CCD camera for the same light sources during the measurement. The pictures were taken at the distance of 80 cm between the CCD camera and a black screen placed at the measurement plane of the scanner. The pictures of flux distribution patterns as shown in Figures 4.4(a) and 4.5(a) are consistent with the measurement results obtained using the optical scanner for both position and irradiance level as shown in Figures 4.4(b) and 4.5(b), respectively. The contour map of light flux distribution can also provide information about the absolute value of the light irradiance level. More detail about the light distribution can be accomplished by choosing a smaller range of light irradiance.

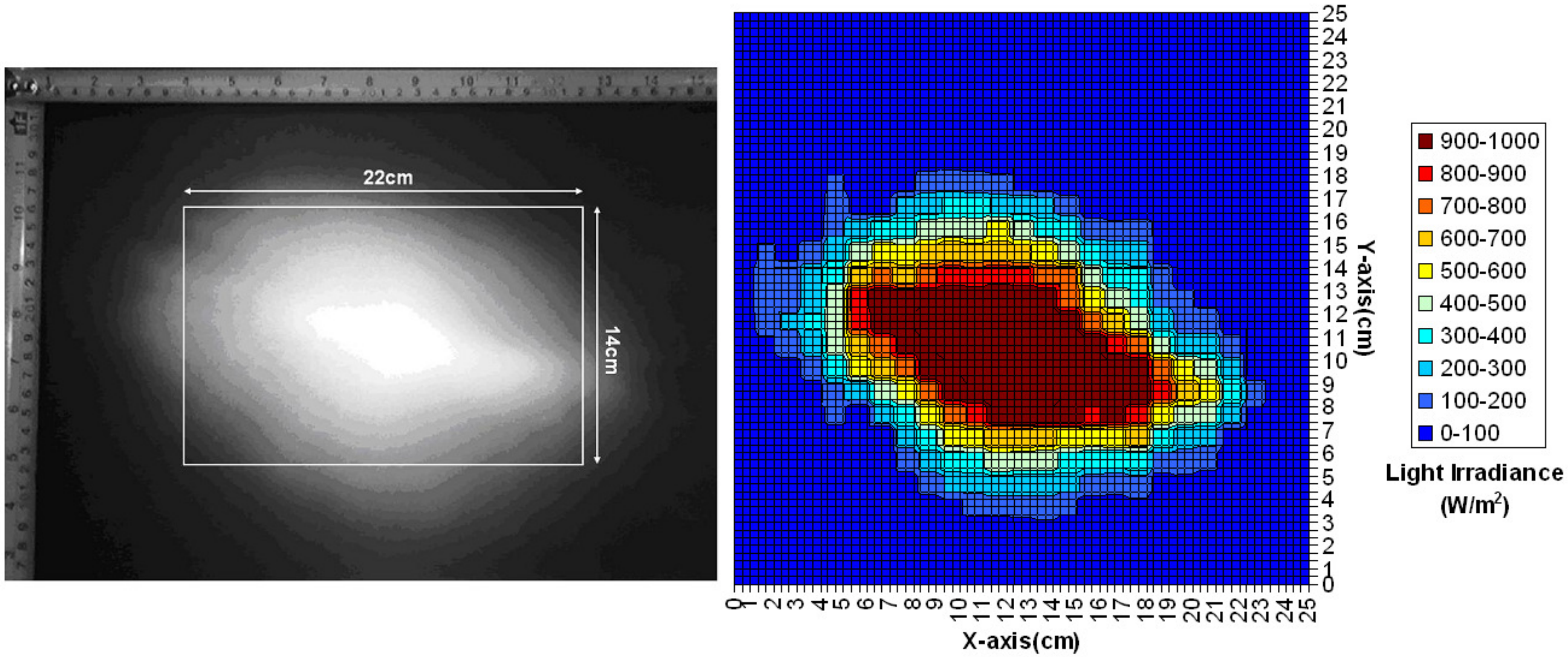

(a) (b)

Figure 4.4: Light flux distribution of the first artificial light source consisted of three motorcycle xenon headlamp of 35 W each: (a) picture taken by a CCD camera, (b) contour map plotted by the optical scanner. The distance between the light source and the scanner was fixed at 50 cm. All the lamps used during the measurement were reasonably new with a total operating time of less than 5 hours.

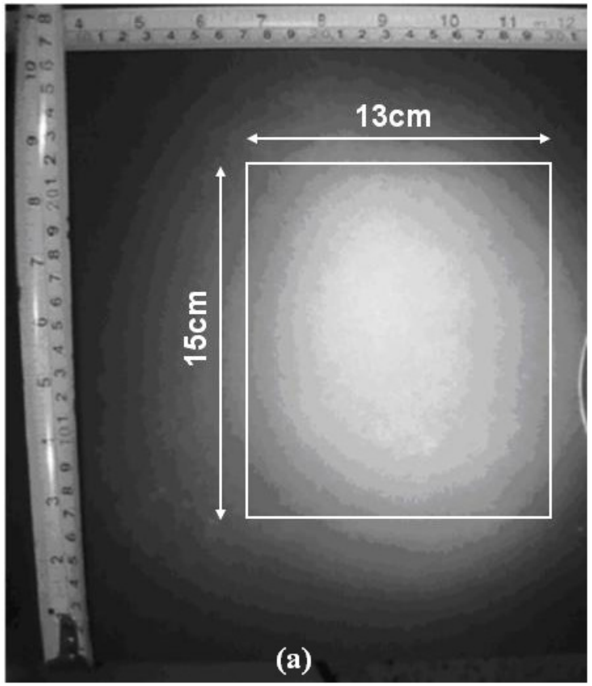

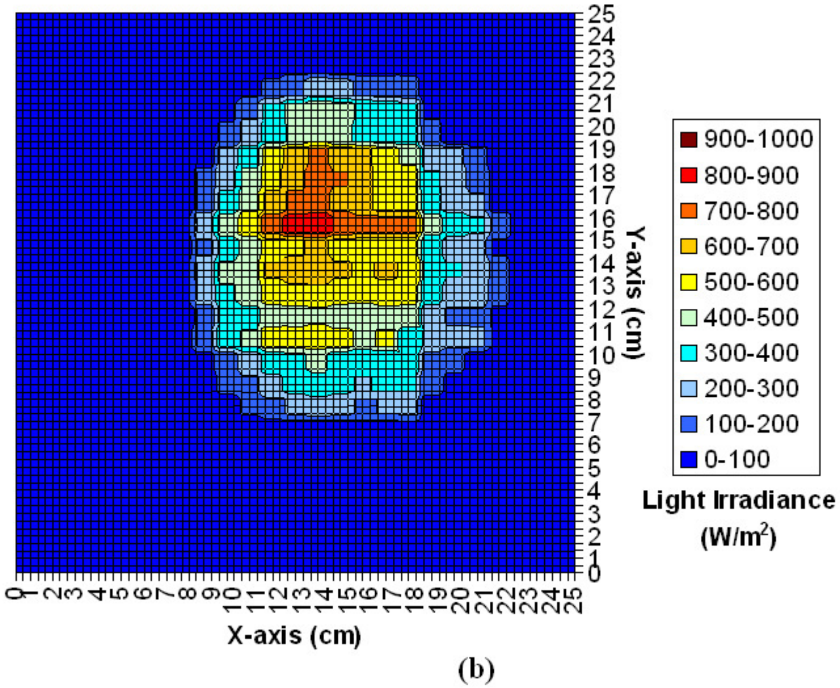

Figure 4.5: Light flux distribution of the second artificial light source comprised of three commercial xenon lamps of 20 W each: (a) picture taken by a CCD camera, (b) contour map plotted by the optical scanner. The distance between the light source and the scanner was fixed at 50 cm. All the lamps used during the measurement were reasonably new with a total operating time of less than 5 hours.

4.2.2 Sunlight

The performance of the optical scanner is also evaluated by using a highly uniform illumination source, sunlight, and therefore the irradiance distribution of sunlight was also acquired and the result are shown in Figure 4.6. With a direct normal irradiance of 752 W/m^2, the flux distribution map in Figure 4.6 has revealed that most of the measurement area exhibited irradiance levels ranging from 700 – 800 W/m^2 except a few locations. However, the overall measurement result was still within the accuracy of the optical scanner, showing a very promising performance of the optical scanner to acquire light irradiance levels from any light source.

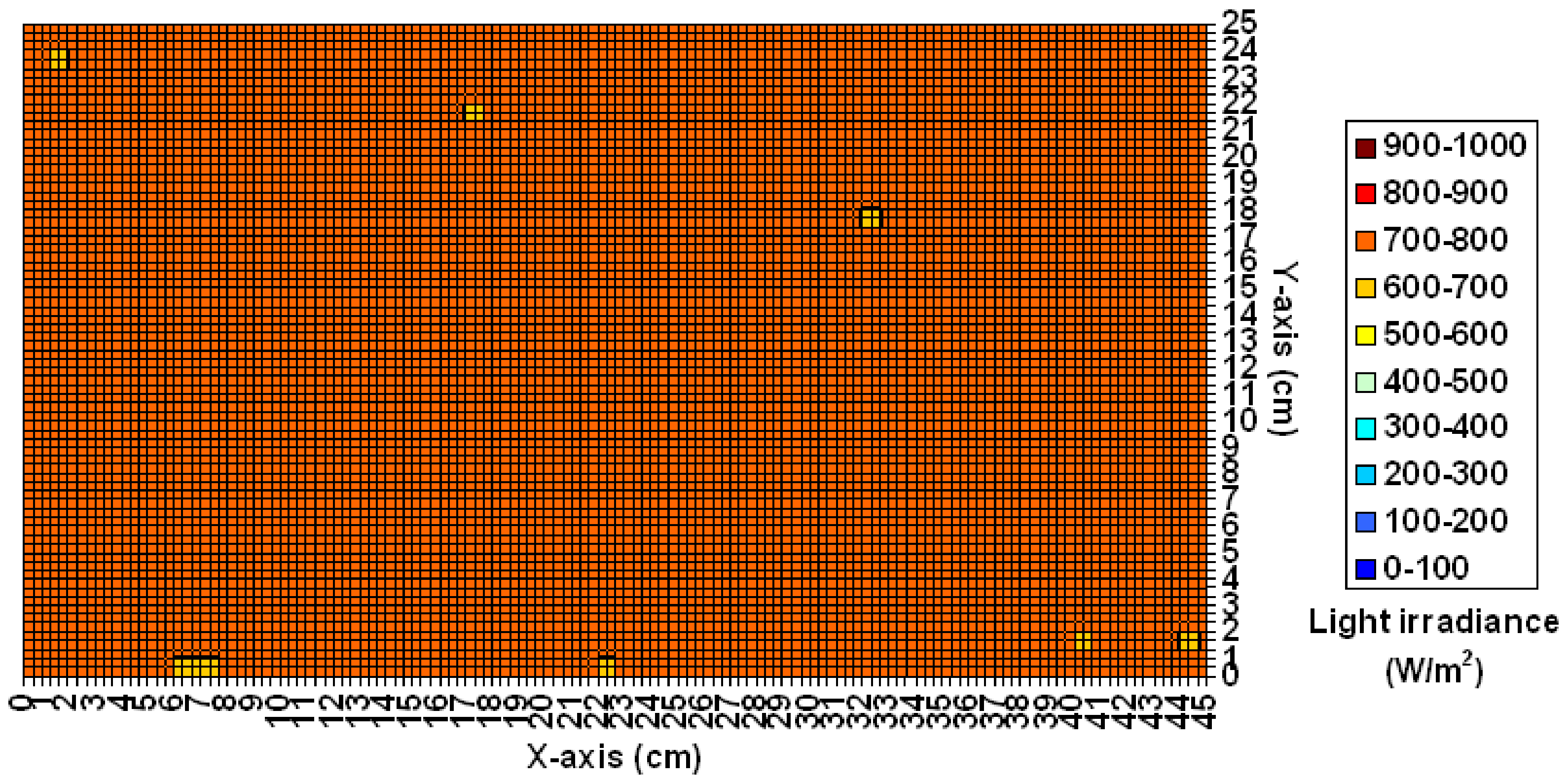

Figure 4.6: Light flux distribution of sunlight with a direct normal irradiance of 752 W/m^2.

4.2.3 Solar Flux Distribution for Different Thickness of Mirror

The solar images reflected by four types of flat mirrors with different dielectric thicknesses on the receiver plane of NIPC prototype were measured in the experiment. The real time solar flux distribution profiles were acquired by using optical scanner that is installed at the receiver plane and at the same time the solar irradiance was also measured with pryheliometer as the reference. Figure 4.7(a)-(d) show the flux distribution maps of solar image from the flat mirrors with thicknesses ranging from 3 mm to 6 mm, which have been installed on the prototype of NIPC as shown in Figure 4.3.

Solar image cast by 6 mm flat mirror has the highest uniformity while solar image reflected by 3 mm flat mirror shows the worst uniformity. To rank the uniformity of solar flux distribution produced by different thicknesses of mirrors, according to the result shown in Figure 4.7, the thicker the mirror the better the uniformity will be. It is reasonable that the thicker mirror with higher mechanical strength can have a better resistant to external force that may deform it during the installation. In our experiment, it also can conclude that the 6 mm mirror is the most suitable thickness to sustain the specular reflection surface and able to produce highly uniform image on the target.

The simulation result in Figure 4.8 shows similar size for the highest illumination area with the measurement result of image reflected by 6mm mirror shown in Figure 4.7(d).

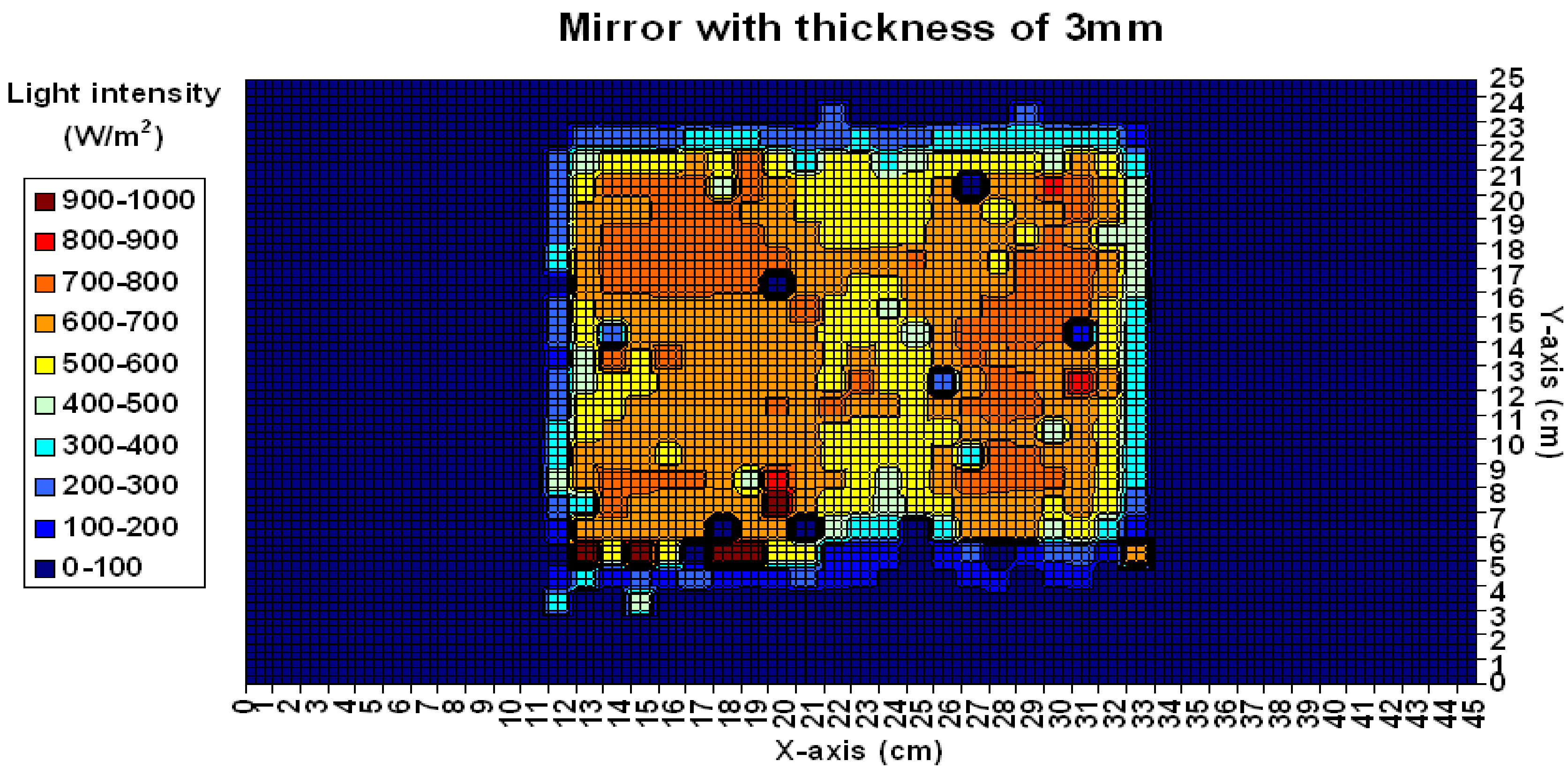

Solar direct normal insolation = 796 W/ m^2

Figure 4.7 (a)

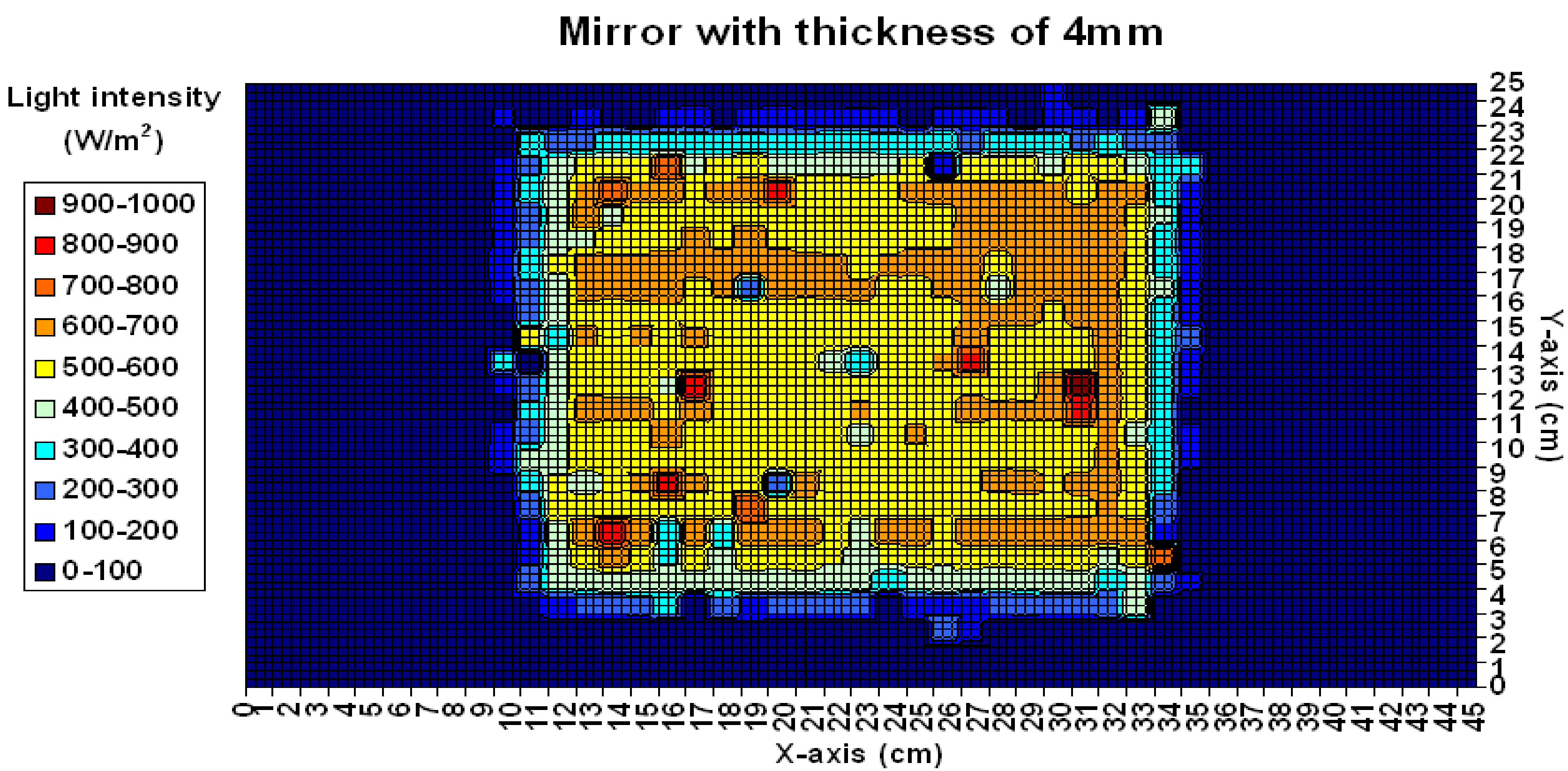

Solar direct normal insolation = 805 W/ m^2

Figure 4.7 (b)

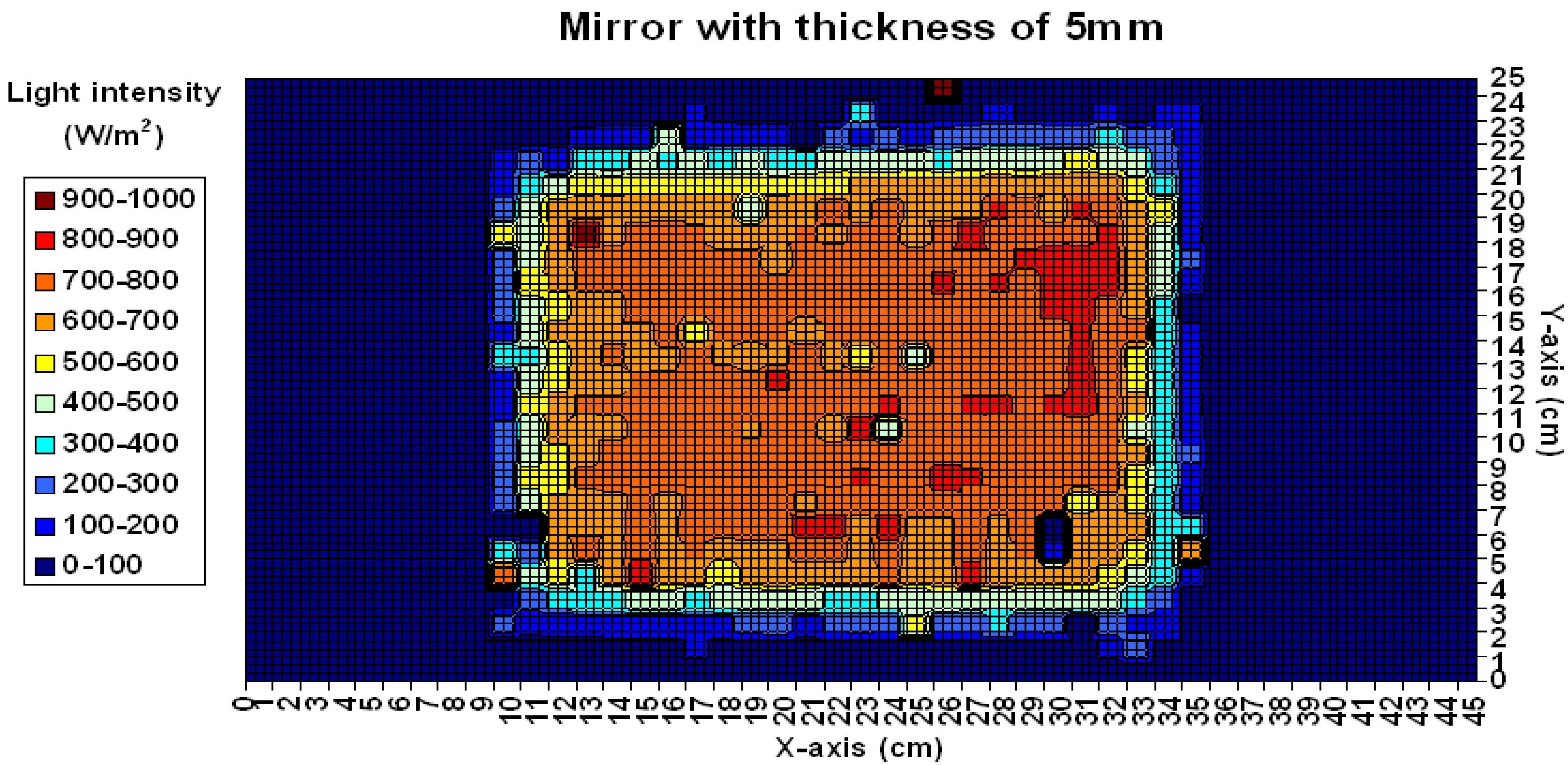

Solar direct normal insolation = 818 W/ m^2

Figure 4.7 (c)

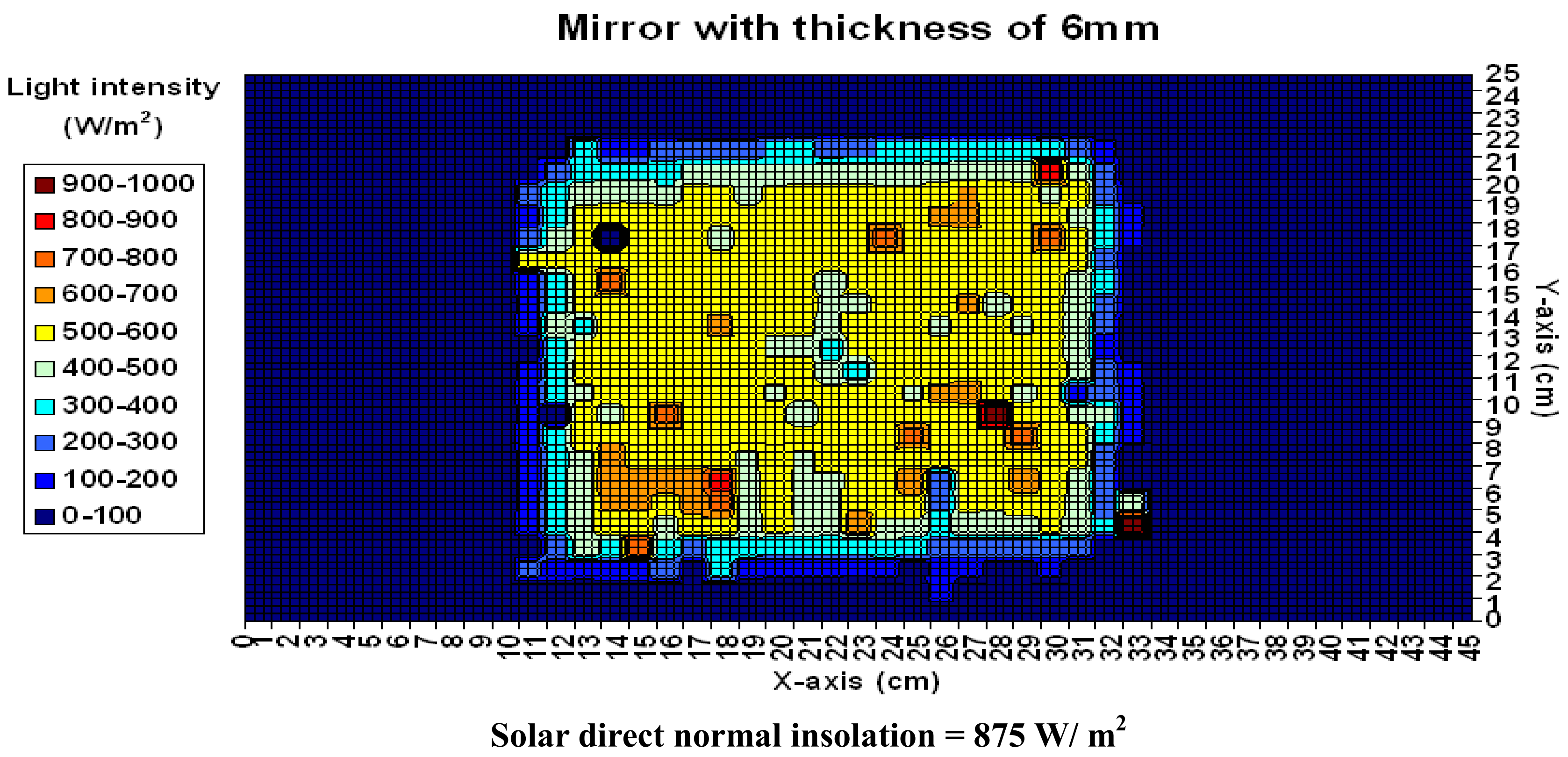

Figure 4.7 (d)

Fig. 4.7: Flux maps show the solar flux distribution of image reflected by mirror with different glass thickness of (a) 3mm, (b) 4mm, (c) 5mm, (d) 6mm.

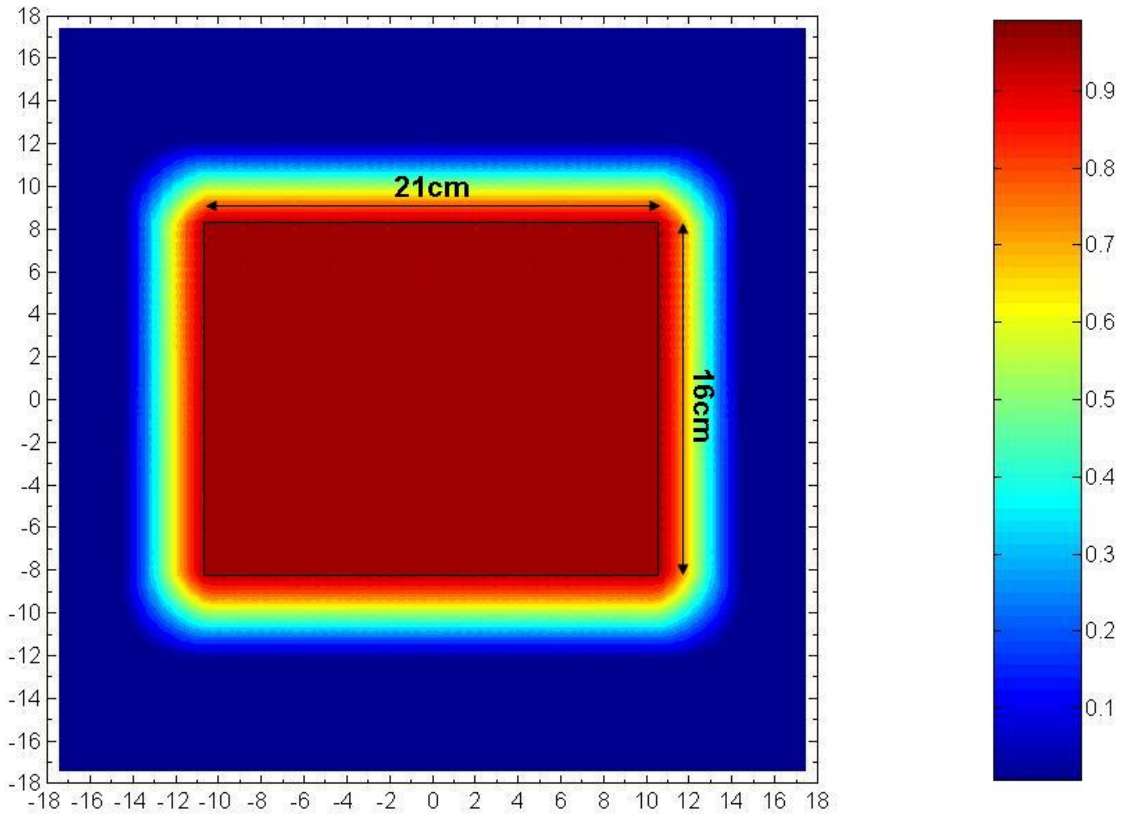

Fig. 4.8: Flux maps from optical simulation show the solar flux distribution of image for a single mirror

CHAPTER 5

DISCUSSION and CONCLUSION

5.1 Discussion

The novel optical scanner has been constructed and tested with artificial light source and sunlight to evaluate the performance. It was later utilized to evaluate the light flux distribution of image reflected by flat mirror which was used in the Non-Imaging Planar Concentrator built in Universiti Tunku Abdul Rahman, Kuala Lumpur, Malaysia.

5.1.1 Trade-offs in terms of Cost, Speed, Accuracy and Type of Light Source

The scanner was built at lower cost but was able to perform measurement and provide outcome same as other commercial light flux mappers. Comparison had been done to study the trade-offs in terms of cost, speed, accuracy and type of light source among three different possible methods for acquiring the light flux distribution map. The comparisons are shown in Table 5.1. For the cost comparison, the estimated cost of a stepper motor and its associated driving components to be US$ 312.50 and the cost of a photodiode at US$ 12.50. The cost estimation of the aforementioned items was based on our cost of setting up the current optical scanner which is able to perform measurement over an area of 45 cm × 25 cm.

	Single photodetector configuration	Single row photodetector configuration	$m \times n$ array of photodetector configuration
Configuration	1 photodiode and 2 stepper motors with associated driving components	25 photodiodes and 1 stepper motor with associated driving component	1125 (or 25 × 45) photodiodes
Estimated cost (US$)	12.5 + (2 × 312.50) = 637.50	(25 × 12.5) + 312.50 = 625.00	1125 × 12.5 = 14,062.50
Data acquisition time	125 second	5 second	< 1 second
Accuracy	Lowest accuracy that is highly relied on the accuracy of 2-D motions of two stepper motors.	Moderate accuracy that is highly relied on the accuracy of 1-D motion of a single stepper motor.	Highest accuracy.
Type of light source	Stable artificial light source	All types of light sources including real time sunlight and artificial light source.	All types of light sources including real time sunlight and artificial light source.

Table 5.1: Comparisons in terms of cost, speed, accuracy and type of light source among three different possible methods of acquiring the light flux distribution map.

From the overall comparison, the single row photodetector configuration fare better that single photodetector configuration and $m \times n$ array of photodetector configuration. Although in a certain aspect the single row photodetector configuration is not the best among the three but it is the most balance configuration when more than one aspect was taken into consideration for the measurement requirement. It only cost a bit more than the single photodetector configuration but is very much faster and accurate. $m \times n$ array of photodetector configuration is able to perform measurement in less than a second but the single row photodetector configuration measurement time 5 second and is considered reasonably fast.

5.1.2 Potential for 3-D Measurements

Since the 3-D measurement device is gaining interest in many applications, it is also possible for the current design to be further upgraded from a 2-D to a 3-D optical scanner by adding an additional motion to the photodiode array in the vertical direction (z-axis). In this case, the data acquisition algorithm has to be modified as well to allow the data collection in three dimensions.

5.1.3 Measurement of Light Flux of Very High Concentration

The optical scanner can be modified to measure the light flux distribution of very high concentration light flux. Concentrator photovoltaic (CPV) cells which can response to thousand concentration of light flux can be used to substitute the photodiodes used for the current optical scanner for very high concentration light flux measurement. An active cooling system must be used to cool down the CPV cells under very high concentration to prevent the cells from damage and to obtain a consistence measurement. The output of CPV cells vary with temperature and thus a cooling system is needed to maintain the temperature of the CPV cells.

5.2 Conclusion

An optical scanner that is capable of plotting the light flux distribution pattern across a two-dimensional surface has been successfully designed and constructed. The advantage of the novel optical scanner is that it can perform direct measurement of high resolution flux distributions in absolute irradiance levels from a light source using a fast scanning speed. The optical scanner can produce almost instantaneous results, using a scanning time of only a few seconds. The scanner can be easily scaled up by adding more photo-sensors and by increasing the length of the sliding bar to cover larger illumination areas. Furthermore, the current photodiodes used in the system can be replaced by different types of sensor, i.e. concentrator photovoltaic cells that respond linearly to high light irradiance so that the highly concentrated light up to a thousand times the irradiance of the sun can also be measured.

Image reflected by thicker mirror shows better uniformity of solar flux distribution. This is due to the higher mechanical strength in the mirror with thicker mirror. Thinner mirror suffered more deformation during the installation on the prototype of NIPC, thus solar flux distribution of image reflected is not uniform. The measurement results were then verified by the simulation result, and the results show good agreement between simulation and measurement. To obtain better uniformity of illumination on the concentrator photovoltaic (CPV) cells to have better performance, the flat mirror with thickness of 6 mm is preferred.

REFERENCES

Adsten, M. (2004). Measurement of radiation distribution on the absorber in an asymmetric CPC collector. *Solar Energy*, vol. 76, no. 1, 199-206.

Arqueros, F., Jiménez, A., Valverde, A. (2003). A novel procedure for the optical characterization of solar concentrators. *Solar energy*, 75, 135-142.

Ballestrín, J. and Monterreal, R. (2004). Hybrid heat flux measurement system for solar central receiver evaluation. *Energy*, vol. 29, no. 5, 915-924.

Both, A.J., Ciolkosz, D.E., Albright, L.D. (2002). Evaluation of light uniformity underneath supplemental lighting systems. *Acta Hort. (ISHS) 580*, 183-190.

Chong, K. K., Wong, C. W., Siaw, F. L., and Yew, T. K. (2010). Optical Characterization of Nonimaging Planar Concentrator for the Application in Concentrator Photovoltaic System. *Journal of Solar Energy Engineering*, vol. 132, no. 1, 011011.

Chong, K.K., Yew, T.K. (2011), "Novel Optical Scanner Using Photodiodes Array for Two-Dimensional Measurement of Light Flux Distribution," *IEEE Transactions on Instrumentation and Measurement*, Accepted for publication.

Coventry, J. and Blakers, A. (2006). Direct measurement and simulation techniques for analysis of radiation flux on a linear PV concentrator. *Progress in Photovoltaics: Research and Applications*, vol. 14, pp. 341-352.

Estrada, C.A., Jaramillo, O.A., Acosta, R., Arancibia-Bulnes, C.A. (2007). Heat transfer analysis in a calorimeter for concentrated solar radiation measurements. *Solar energy*, 81, 1306-1313.

Facão, J. and Oliveira, A. C. (2011). Numerical simulation of a trapezoidal cavity receiver for a linear Fresnel solar collector concentrator. *Renewable Energy*, vol. 36, no. 1, 90-96.

Ferriere, A., Rivoire, B. (2002). An instrument for measuring concentrated solar radiation: A photo-sensor interfaced with an integrating sphere. *Solar energy*, 72, 187-193.

Henjes, C., Frey, H.-U. (2001). Investgation on the Flux Uniformity Depending on the Lamp Pattern of a Solar Simulator. *Proceddings 4th International Symposium on Environmental Testing for Space Programmes*, 515-521.

Jung, W. (2006). *Op Amp applications handbook*, Burlington MA: Newnes, 258-259.

Kamada, Osamu (1964). Method of measuring target temperature in a solar furnace. *Applied optics*, 3, 1397-1400.

Kasap, S.O. (2001). *Optoelectronics and photonics: principles and practices*, Upper Saddle River: Prentice Hall, 217-253.

Leutz, R. and Annen, H. (2007). Reverse ray-tracing model for the performance evaluation of stationary solar concentrators," *Solar Energy*, vol. 81, no. 6, 761-767.

Pancotti, L. (2007). Optical simulation model for flat mirror concentrators. *Solar Energy Materials and Solar Cells*, vol. 91, no. 7, 551-559.

Parr A., Datla R., Gardner J. (2005). *Optical radiometry*. Amsterdam ;Boston: Academic Press. 163-164.

Parretta, A., Privato, C., Nenna, G.., Antonini, A., Stefancich, M. (2006). Monitoring of concentrated radiation bean for photovoltaic and thermal solar energy conversion applications. *Applied optics*, 45, 7885-7897.

Parretta, A., Antonini, A., Armani, M., Nenna, G., Flaminio, G., Pellegrini, M. (2007). Double–cavity radiometer for high-flux density solar radiation measurements. *Applied optics*, 46, 2166-2179.

Pottler, K., Lüpfert, E., Johnston, G.H.G., Shortis, M.R. (2005). Photogrammetry: A powerful tool for geometric analysis of solar concentrators and their components. *Transactions of the ASME*, 127, 94-101.

PV Measurements, Inc. (2009). *Solar Simulator Uniformity Mapper*. URL : http://www.pvmeasurements.com/products/solar-simulator-uniformity-mapper . Accessed on 1st March 2011.

Riffelmann, K.-J., Neumann, A. and Wittkowski, M. (2003). PARASCAN: A New Parabolic Trough Flux Scanner. *Proceedings of ISES Solar World Congress*, Göteborg, Sweden.

Sansoni, P., Francini, F., Fontani, D. (2007). Optical characterization of solar concentrator. *Optical and Laser engineering*, 45, 351-359.

Shuai, Y., Xia, X., and Tan, H. (2008). Numerical Study of Radiation Characteristics in a Dish Solar Collector System. *Journal of Solar Energy Engineering*, vol. 130, no. 2, 021001.

Ulmer, S., Reinalter, W., Heller, P., Lüpfert, E., and Martínez, D. (2002). Beam Characterization and Improvement with a Flux Mapping System for

Dish Concentrators. *Journal of Solar Energy Engineering*, vol. 124, no. 2, 182.

US Resource Assessment (USRA). (2011). *Pyheliometer*. URL: http://usrasolutions.com/?page_id=21 . Accessed on 18th July 2011.

Vandenberg, R., Bolingen, M., and Wieting, R. (1993), What does "one-sun intensity" mean for I-V curve measurement? Intensity-induced errors on different types of large area a-Si modules. *Solar Energy Materials and Solar Cells*, vol. 29, 77-84.

Wilson, J. (2005). *Sensor technology handbook*, Amsterdam: Boston: Elsevier, 108-110.

APPENDIX A

TL084 OPERATIONAL AMPLIFIERS

TL084
TL084A - TL084B

GENERAL PURPOSE J-FET QUAD OPERATIONAL AMPLIFIERS

- WIDE COMMON-MODE (UP TO V_{CC}^{+}) AND DIFFERENTIAL VOLTAGE RANGE
- LOW INPUT BIAS AND OFFSET CURRENT
- OUTPUT SHORT-CIRCUIT PROTECTION
- HIGH INPUT IMPEDANCE J–FET INPUT STAGE
- INTERNAL FREQUENCY COMPENSATION
- LATCH UP FREE OPERATION
- HIGH SLEW RATE : 16V/µs (typ)

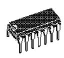

N
DIP14
(Plastic Package)

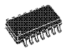

D
SO14
(Plastic Micropackage)

P
TSSOP14
(Thin Shrink Small Outline Package)

ORDER CODE

Part Number	Temperature Range	Package		
		N	D	P
TL084M/AM/BM	-55°C, +125°C	•	•	•
TL084I/AI/BI	-40°C, +105°C	•	•	•
TL084C/AC/BC	0°C, +70°C	•	•	•
Example : TL084CN, TL084CD				

N = Dual in Line Package (DIP)
D = Small Outline Package (SO) - also available in Tape & Reel (DT)
P = Thin Shrink Small Outline Package (TSSOP) - only available in Tape & Reel (PT)

DESCRIPTION

The TL084, TL084A and TL084B are high speed J–FET input quad operational amplifiers incorporating well matched, high voltage J–FET and bipolar transistors in a monolithic integrated circuit.

The devices feature high slew rates, low input bias and offset currents, and low offset voltage temperature coefficient.

PIN CONNECTIONS (top view)

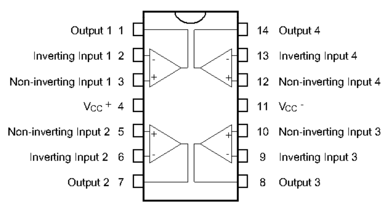

March 2001 1/12

ELECTRICAL CHARACTERISTICS

V_{CC} = ±15V, T_{amb} = +25°C (unless otherwise specified)

Symbol	Parameter	TL084I,M,AC,AI,AM, BC,BI,BM			TL084C			Unit
		Min.	Typ.	Max.	Min.	Typ.	Max.	
V_{io}	Input Offset Voltage (R_s = 50Ω) T_{amb} = +25°C TL084 TL084A TL084B $T_{min} \le T_{amb} \le T_{max}$ TL084 TL084A TL084B		 3 3 1	 10 6 3 13 7 5		 3 13	 10 13	mV
DV_{io}	Input Offset Voltage Drift		10			10		μV/°C
I_{io}	Input Offset Current - note 1) T_{amb} = +25°C $T_{min} \le T_{amb} \le T_{max}$		 5	 100 4		 5	 100 4	 pA nA
I_{ib}	Input Bias Current -note 1 T_{amb} = +25°C $T_{min} \le T_{amb} \le T_{max}$		 20	 200 20		 20	 400 20	 pA nA
A_{vd}	Large Signal Voltage Gain (R_L = 2kΩ, V_o = ±10V) T_{amb} = +25°C $T_{min} \le T_{amb} \le T_{max}$	 50 25	 200		 25 15	 200		V/mV
SVR	Supply Voltage Rejection Ratio (R_S = 50Ω) T_{amb} = +25°C $T_{min} \le T_{amb} \le T_{max}$	 80 80	 86		 70 70	 86		dB
I_{CC}	Supply Current, no load, per amplifier T_{amb} = +25°C $T_{min} \le T_{amb} \le T_{max}$		 1.4	 2.5 2.5		 1.4	 2.5 2.5	mA
V_{icm}	Input Common Mode Voltage Range	±11	+15 -12		±11	+15 -12		V
CMR	Common Mode Rejection Ratio (R_S = 50Ω) T_{amb} = +25°C $T_{min} \le T_{amb} \le T_{max}$	 80 80	 86		 70 70	 86		dB
I_{os}	Output Short-circuit Current T_{amb} = +25°C $T_{min} \le T_{amb} \le T_{max}$	 10 10	 40	 60 60	 10 10	 40	 60 60	mA
$\pm V_{opp}$	Output Voltage Swing T_{amb} = +25°C RL = 2kΩ RL = 10kΩ $T_{min} \le T_{amb} \le T_{max}$ RL = 2kΩ RL = 10kΩ	 10 12 10 12	 12 13.5		 10 12 10 12	 12 13.5		V
SR	Slew Rate (T_{amb} = +25°C) V_{in} = 10V, R_L = 2kΩ, C_L = 100pF, unity gain	 8	 16		 8	 16		V/μs
t_r	Rise Time (T_{amb} = +25°C) V_{in} = 20mV, R_L = 2kΩ, C_L = 100pF, unity gain		 0.1			 0.1		μs
K_{ov}	Overshoot (T_{amb} = +25°C) V_{in} = 20mV, R_L = 2kΩ, C_L = 100pF, unity gain		 10			 10		%
GBP	Gain Bandwidth Product (T_{amb} = +25°C) V_{in} = 10mV, R_L = 2kΩ, C_L = 100pF, f= 100kHz	 2.5	 4		 2.5	 4		MHz
R_i	Input Resistance		10^{12}			10^{12}		Ω

Symbol	Parameter	TL084I,M,AC,AI,AM, BC,BI,BM			TL084C			Unit
		Min.	Typ.	Max.	Min.	Typ.	Max.	
THD	Total Harmonic Distortion (T_{amb} = +25°C), f= 1kHz, R_L = 2kΩ, C_L = 100pF, A_v = 20dB, V_o = $2V_{pp}$		0.01			0.01		%
e_n	Equivalent Input Noise Voltage R_S = 100Ω, f = 1KHz		15			15		$\frac{nV}{\sqrt{Hz}}$
∅m	Phase Margin		45			45		degrees
V_{o1}/V_{o2}	Channel Separation A_v = 100		120			120		dB

1. The input bias currents are junction leakage currents which approximately double for every 10°C increase in the junction temperature.

APPENDIX B

HCF4053B ANALOG MULTIPLEXER

HCF4053B

TRIPLE 2-CHANNEL ANALOG MULTIPLEXER/DEMULTIPLEXER

- LOW "ON" RESISTANCE : 125Ω (Typ.) OVER 15V p.p SIGNAL-INPUT RANGE FOR V_{DD} - V_{EE} = 15V
- HIGH "OFF" RESISTANCE : CHANNEL LEAKAGE ± 100pA (Typ.) at V_{DD} - V_{EE} = 18V
- BINARY ADDRESS DECODING ON CHIP
- HIGH DEGREE OF LINEARITY : < 0.5% DISTORTION TYP. at f_{IS} = 1KHz, V_{IS} = 5 V_{pp}, V_{DD} - V_{SS} ≥ 10V, RL = 10KΩ
- VERY LOW QUIESCENT POWER DISSIPATION UNDER ALL DIGITAL CONTROL INPUT AND SUPPLY CONDITIONS : 0.2 μW (Typ.) at V_{DD} - V_{SS} = V_{DD} - V_{EE} =10V
- MATCHED SWITCH CHARACTERISTICS : R_{ON} = 5Ω (Typ.) FOR V_{DD} - V_{EE} = 15V
- WIDE RANGE OF DIGITAL AND ANALOG SIGNAL LEVELS : DIGITAL 3 to 20, ANALOG TO 20V p.p.
- QUIESCENT CURRENT SPECIF. UP TO 20V
- 5V, 10V AND 15V PARAMETRIC RATINGS
- INPUT LEAKAGE CURRENT I_I = 100nA (MAX) AT V_{DD} = 18V T_A = 25°C
- 100% TESTED FOR QUIESCENT CURRENT
- MEETS ALL REQUIREMENTS OF JEDEC JESD13B " STANDARD SPECIFICATIONS FOR DESCRIPTION OF B SERIES CMOS DEVICES"

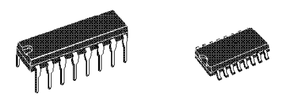

ORDER CODES

PACKAGE	TUBE	T & R
DIP	HCF4053BEY	
SOP	HCF4053BM1	HCF4053M013TR

DESCRIPTION

The HCF4053B is a monolithic integrated circuit fabricated in Metal Oxide Semiconductor technology available in DIP and SOP packages.
The HCF4053B analog multiplexer/demultiplexer is a digitally controlled analog switch having low ON impedance and very low OFF leakage current. This multiplexer circuit dissipate extremely low quiescent power over the full V_{DD} - V_{SS} and V_{DD} - V_{EE} supply voltage range, independent of the logic state of the control signals.
When a logic "1" is present at the inhibit input terminal all channel are off. This device is a triple 2-channel multiplexer having three separate digital control inputs, A, B, and C, and an inhibit input. Each control input selects one of a pair of channels which are connected in a single pole double-throw configuration.

PIN CONNECTION

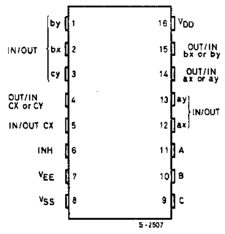

DC SPECIFICATIONS

Symbol	Parameter	Test Condition				Value							Unit
		V_{IS} (V)	V_{EE} (V)	V_{SS} (V)	V_{DD} (V)	T_A = 25°C			-40 to 85°C		-55 to 125°C		
						Min.	Typ.	Max.	Min.	Max.	Min.	Max.	
I_L	Quiescent Device Current (all switches ON or all switches OFF)				5		0.04	5		150		150	μA
					10		0.04	10		300		300	
					15		0.04	20		600		600	
					20		0.08	100		3000		3000	
SWITCH													
R_{ON}	Resistance	$0 \leq V_I \leq V_{DD}$	0	0	5		470	1050		1200		1200	Ω
					10		180	400		520		520	
					15		125	280		360		360	
Δ_{ON}	Resistance Δ_{RON} (between any 2 of 4 switches)	$0 \leq V_I \leq V_{DD}$	0	0	5		10						Ω
					10		10						
					15		5						
OFF*	Channel Leakage Current (All Channel OFF) (COMMON O/I)		0	0	18		±0.1	100		1000		1000	nA
OFF*	Channel Leakage Current (Any Channel OFF)		0	0	18		±0.1	100		1000		1000	nA
C_I	Input Capacitance		-5	-5	5		5						pF
C_O	Output Capacitance						9						
C_{IO}	Feed through						0.2						
CONTROL (Address or Inhibit)													
V_{IL}	Input Low Voltage	= VDD thru 1KΩ	$V_{EE} = V_{SS}$ R_L = 1KΩ to V_{SS} $I_{IS} < 2\mu A$ (on all OFF channels)		5			1.5		1.5		1.5	V
					10			3		3		3	
					15			4		4		4	
V_{IH}	Input High Voltage				5	3.5			3.5		3.5		V
					10	7			7		7		
					15	11			11		11		
I_{IH}, I_{IL}	Input Leakage Current	V_I = 0/18V			18		$\pm 10^{-3}$	±0.1		±1		±1	μA
C_I	Input Capacitance						5	7.5					pF

* Determined by minimum feasible leakage measurement for automating testing.

DYNAMIC ELECTRICAL CHARACTERISTICS (T_{amb} = 25°C, C_L = 50pF, all input square wave rise and fall time = 20 ns)

Parameter	Test Condition							Value			Unit
	V_{EE} (V)	**R_L** (KΩ)	**f_I** (KHz)	**V_I** (V)	**V_{SS}** (V)	**V_{DD}** (V)		**Min.**	**Typ.**	**Max.**	
Propagation Delay Time (signal input to output)		200		V_{DD}		5			30	60	ns
						10			15	30	
						15			11	20	
Frequency Response Channel "ON" (sine wave input) at 20 log V_O/V_I = - 3dB	= V_{SS}	1		5(*)		10	V_O at Common OUT/IN		25		MHz
							V_O at any channel		60		
Feed through (all channels OFF) at 20 log V_O/V_I = - 40dB	= V_{SS}	1		5(*)		10	V_O at Common OUT/IN		10		MHz
							V_O at any channel		8		
Frequency Signal Crosstalk at 20 log V_O/V_I = -40dB	= V_{SS}	1		5(*)		10	Between any 2 Sections (IN pin 2, OUT pin 14)		2.5		MHz
							Between any 2 Sections (IN pin 15, OUT pin 14)		6		
Sine Wave Distortion f_{IS} = 1KHz Sine Wave	= V_{SS}	10	1	2(*)		5			0.3		%
				3(*)		10			0.2		
				5(*)		15			0.12		
CONTROL (Address or Inhibit)											
Propagation Delay: Address to Signal OUT (Channels ON or OFF)	0				0	5			360	720	ns
	0				0	10			160	320	
	0				0	15			120	240	
	-5				0	5			225	450	
Propagation Delay: Inhibit to Signal OUT (Channel turning ON)	0	1			0	5			360	720	ns
	0				0	10			160	320	
	0				0	15			120	240	
	-10				0	5			200	400	
Propagation Delay: Inhibit to Signal OUT (Channel turning OFF)	0	10				5			200	450	ns
	0					10			90	210	
	0					15			70	160	
	-10					5			130	300	
Address or Inhibit to Signal Crosstalk	0	10 (1)			0	10	$V_C = V_{DD}-V_{SS}$ (square wave)		65		mV peak

(1) Both ends of channel.
* Peak to Peak voltage symmetrical about (V_{DD} - V_{EE}) /2

APPENDIX C

PIC18F4550 44-PIN USB MICROCONTROLLERS

MICROCHIP **PIC18F2455/2550/4455/4550**

28/40/44-Pin, High-Performance, Enhanced Flash, USB Microcontrollers with nanoWatt Technology

Universal Serial Bus Features:

- USB V2.0 Compliant
- Low Speed (1.5 Mb/s) and Full Speed (12 Mb/s)
- Supports Control, Interrupt, Isochronous and Bulk Transfers
- Supports up to 32 Endpoints (16 bidirectional)
- 1-Kbyte Dual Access RAM for USB
- On-Chip USB Transceiver with On-Chip Voltage Regulator
- Interface for Off-Chip USB Transceiver
- Streaming Parallel Port (SPP) for USB streaming transfers (40/44-pin devices only)

Power-Managed Modes:

- Run: CPU on, peripherals on
- Idle: CPU off, peripherals on
- Sleep: CPU off, peripherals off
- Idle mode currents down to 5.8 μA typical
- Sleep mode currents down to 0.1 μA typical
- Timer1 Oscillator: 1.1 μA typical, 32 kHz, 2V
- Watchdog Timer: 2.1 μA typical
- Two-Speed Oscillator Start-up

Flexible Oscillator Structure:

- Four Crystal modes, including High Precision PLL for USB
- Two External Clock modes, up to 48 MHz
- Internal Oscillator Block:
  - 8 user-selectable frequencies, from 31 kHz to 8 MHz
  - User-tunable to compensate for frequency drift
- Secondary Oscillator using Timer1 @ 32 kHz
- Dual Oscillator options allow microcontroller and USB module to run at different clock speeds
- Fail-Safe Clock Monitor:
  - Allows for safe shutdown if any clock stops

Peripheral Highlights:

- High-Current Sink/Source: 25 mA/25 mA
- Three External Interrupts
- Four Timer modules (Timer0 to Timer3)
- Up to 2 Capture/Compare/PWM (CCP) modules:
  - Capture is 16-bit, max. resolution 5.2 ns ($T_{CY}/16$)
  - Compare is 16-bit, max. resolution 83.3 ns (T_{CY})
  - PWM output: PWM resolution is 1 to 10-bit
- Enhanced Capture/Compare/PWM (ECCP) module:
  - Multiple output modes
  - Selectable polarity
  - Programmable dead time
  - Auto-shutdown and auto-restart
- Enhanced USART module:
  - LIN bus support
- Master Synchronous Serial Port (MSSP) module supporting 3-wire SPI (all 4 modes) and I^2C™ Master and Slave modes
- 10-bit, up to 13-channel Analog-to-Digital Converter module (A/D) with Programmable Acquisition Time
- Dual Analog Comparators with Input Multiplexing

Special Microcontroller Features:

- C Compiler Optimized Architecture with optional Extended Instruction Set
- 100,000 Erase/Write Cycle Enhanced Flash Program Memory typical
- 1,000,000 Erase/Write Cycle Data EEPROM Memory typical
- Flash/Data EEPROM Retention: > 40 years
- Self-Programmable under Software Control
- Priority Levels for Interrupts
- 8 x 8 Single-Cycle Hardware Multiplier
- Extended Watchdog Timer (WDT):
  - Programmable period from 41 ms to 131s
- Programmable Code Protection
- Single-Supply 5V In-Circuit Serial Programming™ (ICSP™) via two pins
- In-Circuit Debug (ICD) via two pins
- Optional dedicated ICD/ICSP port (44-pin devices only)
- Wide Operating Voltage Range (2.0V to 5.5V)

Device	Program Memory		Data Memory		I/O	10-Bit A/D (ch)	CCP/ECCP (PWM)	SPP	MSSP		EAUSART	Comparators	Timers 8/16-Bit
	Flash (bytes)	# Single-Word Instructions	SRAM (bytes)	EEPROM (bytes)					SPI	Master I^2C™			
PIC18F2455	24K	12288	2048	256	24	10	2/0	No	Y	Y	1	2	1/3
PIC18F2550	32K	16384	2048	256	24	10	2/0	No	Y	Y	1	2	1/3
PIC18F4455	24K	12288	2048	256	35	13	1/1	Yes	Y	Y	1	2	1/3
PIC18F4550	32K	16384	2048	256	35	13	1/1	Yes	Y	Y	1	2	1/3

 Preliminary

1.0 DEVICE OVERVIEW

This document contains device-specific information for the following devices:

- PIC18F2455
- PIC18F2550
- PIC18F4455
- PIC18F4550
- PIC18LF2455
- PIC18LF2550
- PIC18LF4455
- PIC18LF4550

This family of devices offers the advantages of all PIC18 microcontrollers – namely, high computational performance at an economical price – with the addition of high endurance, Enhanced Flash program memory. In addition to these features, the PIC18F2455/2550/4455/4550 family introduces design enhancements that make these microcontrollers a logical choice for many high-performance, power sensitive applications.

1.1 New Core Features

1.1.1 nanoWatt TECHNOLOGY

All of the devices in the PIC18F2455/2550/4455/4550 family incorporate a range of features that can significantly reduce power consumption during operation. Key items include:

- **Alternate Run Modes:** By clocking the controller from the Timer1 source or the internal oscillator block, power consumption during code execution can be reduced by as much as 90%.
- **Multiple Idle Modes:** The controller can also run with its CPU core disabled but the peripherals still active. In these states, power consumption can be reduced even further, to as little as 4% of normal operation requirements.
- **On-the-Fly Mode Switching:** The power-managed modes are invoked by user code during operation, allowing the user to incorporate power-saving ideas into their application's software design.
- **Low Consumption in Key Modules:** The power requirements for both Timer1 and the Watchdog Timer are minimized. See **Section 28.0 "Electrical Characteristics"** for values.

1.1.2 UNIVERSAL SERIAL BUS (USB)

Devices in the PIC18F2455/2550/4455/4550 family incorporate a fully featured Universal Serial Bus communications module that is compliant with the USB Specification Revision 2.0. The module supports both low-speed and full-speed communication for all supported data transfer types. It also incorporates its own on-chip transceiver and 3.3V regulator and supports the use of external transceivers and voltage regulators.

1.1.3 MULTIPLE OSCILLATOR OPTIONS AND FEATURES

All of the devices in the PIC18F2455/2550/4455/4550 family offer twelve different oscillator options, allowing users a wide range of choices in developing application hardware. These include:

- Four Crystal modes using crystals or ceramic resonators.
- Four External Clock modes, offering the option of using two pins (oscillator input and a divide-by-4 clock output) or one pin (oscillator input, with the second pin reassigned as general I/O).
- An internal oscillator block which provides an 8 MHz clock (±2% accuracy) and an INTRC source (approximately 31 kHz, stable over temperature and V_{DD}), as well as a range of 6 user-selectable clock frequencies, between 125 kHz to 4 MHz, for a total of 8 clock frequencies. This option frees an oscillator pin for use as an additional general purpose I/O.
- A Phase Lock Loop (PLL) frequency multiplier, available to both the High-Speed Crystal and External Oscillator modes, which allows a wide range of clock speeds from 4 MHz to 48 MHz.
- Asynchronous dual clock operation, allowing the USB module to run from a high-frequency oscillator while the rest of the microcontroller is clocked from an internal low-power oscillator.

Besides its availability as a clock source, the internal oscillator block provides a stable reference source that gives the family additional features for robust operation:

- **Fail-Safe Clock Monitor:** This option constantly monitors the main clock source against a reference signal provided by the internal oscillator. If a clock failure occurs, the controller is switched to the internal oscillator block, allowing for continued low-speed operation or a safe application shutdown.
- **Two-Speed Start-up:** This option allows the internal oscillator to serve as the clock source from Power-on Reset, or wake-up from Sleep mode, until the primary clock source is available.

1.2 Other Special Features

- **Memory Endurance:** The Enhanced Flash cells for both program memory and data EEPROM are rated to last for many thousands of erase/write cycles – up to 100,000 for program memory and 1,000,000 for EEPROM. Data retention without refresh is conservatively estimated to be greater than 40 years.
- **Self-Programmability:** These devices can write to their own program memory spaces under internal software control. By using a bootloader routine, located in the protected Boot Block at the top of program memory, it becomes possible to create an application that can update itself in the field.
- **Extended Instruction Set:** The PIC18F2455/2550/4455/4550 family introduces an optional extension to the PIC18 instruction set, which adds 8 new instructions and an Indexed Literal Offset Addressing mode. This extension, enabled as a device configuration option, has been specifically designed to optimize re-entrant application code originally developed in high-level languages such as C.
- **Enhanced CCP Module:** In PWM mode, this module provides 1, 2 or 4 modulated outputs for controlling half-bridge and full-bridge drivers. Other features include auto-shutdown for disabling PWM outputs on interrupt or other select conditions and auto-restart to reactivate outputs once the condition has cleared.
- **Enhanced Addressable USART:** This serial communication module is capable of standard RS-232 operation and provides support for the LIN bus protocol. Other enhancements include Automatic Baud Rate Detection and a 16-bit Baud Rate Generator for improved resolution. When the microcontroller is using the internal oscillator block, the EUSART provides stable operation for applications that talk to the outside world without using an external crystal (or its accompanying power requirement).
- **10-Bit A/D Converter:** This module incorporates programmable acquisition time, allowing for a channel to be selected and a conversion to be initiated, without waiting for a sampling period and thus, reducing code overhead.
- **Dedicated ICD/ICSP Port:** These devices introduce the use of debugger and programming pins that are not multiplexed with other micro-controller features. Offered as an option in select packages, this feature allows users to develop I/O intensive applications while retaining the ability to program and debug in the circuit.

1.3 Details on Individual Family Members

Devices in the PIC18F2455/2550/4455/4550 family are available in 28-pin and 40/44-pin packages. Block diagrams for the two groups are shown in Figure 1-1 and Figure 1-2.

The devices are differentiated from each other in six ways:

1. Flash program memory (24 Kbytes for PIC18FX455 devices, 32 Kbytes for PIC18FX550).
2. A/D channels (10 for 28-pin devices, 13 for 40/44-pin devices).
3. I/O ports (3 bidirectional ports and 1 input only port on 28-pin devices, 5 bidirectional ports on 40/44-pin devices).
4. CCP and Enhanced CCP implementation (28-pin devices have two standard CCP modules, 40/44-pin devices have one standard CCP module and one ECCP module).
5. Streaming Parallel Port (present only on 40/44-pin devices).

All other features for devices in this family are identical. These are summarized in Table 1-1.

The pinouts for all devices are listed in Table 1-2 and Table 1-3.

Like all Microchip PIC18 devices, members of the PIC18F2455/2550/4455/4550 family are available as both standard and low-voltage devices. Standard devices with Enhanced Flash memory, designated with an "F" in the part number (such as PIC18**F**2550), accommodate an operating V_{DD} range of 4.2V to 5.5V. Low-voltage parts, designated by "LF" (such as PIC18**LF**2550), function over an extended V_{DD} range of 2.0V to 5.5V.

TABLE 1-1: DEVICE FEATURES

Features	PIC18F2455	PIC18F2550	PIC18F4455	PIC18F4550
Operating Frequency	DC – 48 MHz	DC – 48 MHz	DC – 48 MHz	DC – 48 MHz
Program Memory (Bytes)	24576	32768	24576	32768
Program Memory (Instructions)	12288	16384	12288	16384
Data Memory (Bytes)	2048	2048	2048	2048
Data EEPROM Memory (Bytes)	256	256	256	256
Interrupt Sources	19	19	20	20
I/O Ports	Ports A, B, C, (E)	Ports A, B, C, (E)	Ports A, B, C, D, E	Ports A, B, C, D, E
Timers	4	4	4	4
Capture/Compare/PWM Modules	2	2	1	1
Enhanced Capture/ Compare/PWM Modules	0	0	1	1
Serial Communications	MSSP, Enhanced USART	MSSP, Enhanced USART	MSSP, Enhanced USART	MSSP, Enhanced USART
Universal Serial Bus (USB) Module	1	1	1	1
Streaming Parallel Port (SPP)	No	No	Yes	Yes
10-Bit Analog-to-Digital Module	10 Input Channels	10 Input Channels	13 Input Channels	13 Input Channels
Comparators	2	2	2	2
Resets (and Delays)	POR, BOR, RESET Instruction, Stack Full, Stack Underflow (PWRT, OST), MCLR (optional), WDT	POR, BOR, RESET Instruction, Stack Full, Stack Underflow (PWRT, OST), MCLR (optional), WDT	POR, BOR, RESET Instruction, Stack Full, Stack Underflow (PWRT, OST), MCLR (optional), WDT	POR, BOR, RESET Instruction, Stack Full, Stack Underflow (PWRT, OST), MCLR (optional), WDT
Programmable Low-Voltage Detect	Yes	Yes	Yes	Yes
Programmable Brown-out Reset	Yes	Yes	Yes	Yes
Instruction Set	75 Instructions; 83 with Extended Instruction Set enabled	75 Instructions; 83 with Extended Instruction Set enabled	75 Instructions; 83 with Extended Instruction Set enabled	75 Instructions; 83 with Extended Instruction Set enabled
Packages	28-pin PDIP 28-pin SOIC	28-pin PDIP 28-pin SOIC	40-pin PDIP 44-pin QFN 44-pin TQFP	40-pin PDIP 44-pin QFN 44-pin TQFP

FIGURE 1-2: PIC18F4455/4550 (40/44-PIN) BLOCK DIAGRAM

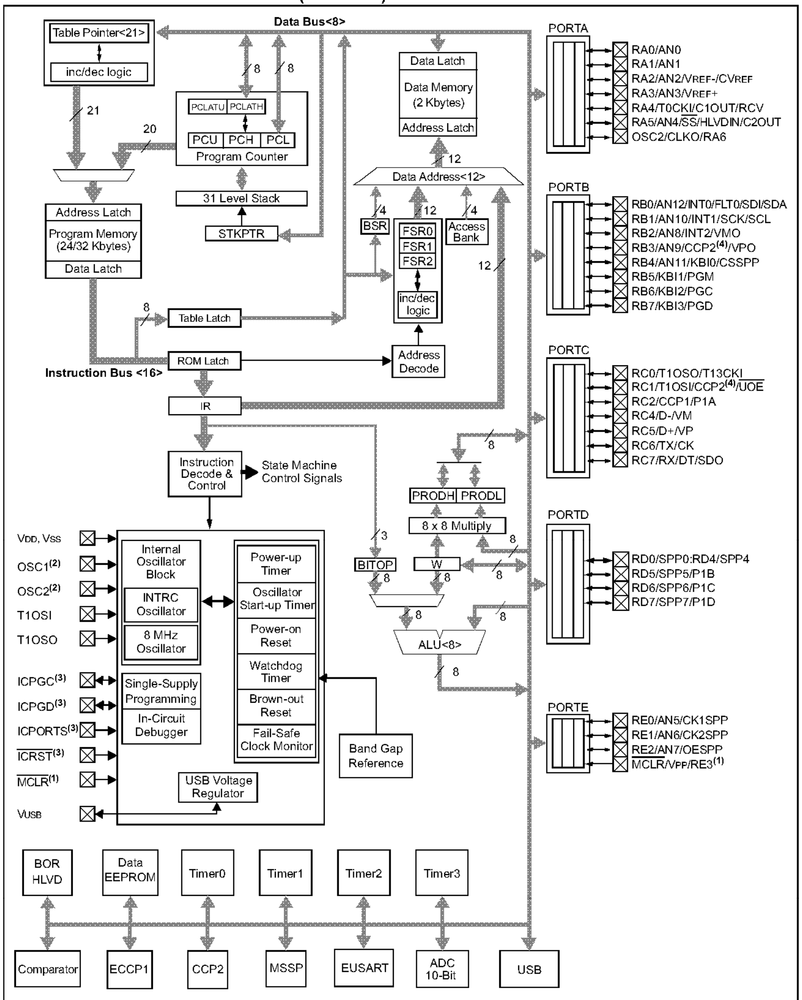

Note 1: RE3 is multiplexed with $\overline{MCLR}$ and is only available when the $\overline{MCLR}$ Resets are disabled.

2: OSC1/CLKI and OSC2/CLKO are only available in select oscillator modes and when these pins are not being used as digital I/O. Refer to **Section 2.0 "Oscillator Configurations"** for additional information.

3: These pins are only available on 44-pin TQFP packages under certain conditions. Refer to **Section 25.9 "Special ICPORT Features (Designated Packages Only)"** for additional information.

4: RB3 is the alternate pin for CCP2 multiplexing.

17.0 UNIVERSAL SERIAL BUS (USB)

This section describes the details of the USB peripheral. Because of the very specific nature of the module, knowledge of USB is expected. Some high-level USB information is provided in **Section 17.10 "Overview of USB"** only for application design reference. Designers are encouraged to refer to the official specification published by the USB Implementers Forum (USB-IF) for the latest information. USB Specification Revision 2.0 is the most current specification at the time of publication of this document.

17.1 Overview of the USB Peripheral

The PIC18FX455/X550 device family contains a full-speed and low-speed compatible USB Serial Interface Engine (SIE) that allows fast communication between any USB host and the PIC® microcontroller.

The SIE can be interfaced directly to the USB, utilizing the internal transceiver, or it can be connected through an external transceiver. An internal 3.3V regulator is also available to power the internal transceiver in 5V applications.

Some special hardware features have been included to improve performance. Dual port memory in the device's data memory space (USB RAM) has been supplied to share direct memory access between the microcontroller core and the SIE. Buffer descriptors are also provided, allowing users to freely program endpoint memory usage within the USB RAM space. A Streaming Parallel Port has been provided to support the uninterrupted transfer of large volumes of data, such as isochronous data, to external memory buffers.

Figure 17-1 presents a general overview of the USB peripheral and its features.

FIGURE 17-1: USB PERIPHERAL AND OPTIONS

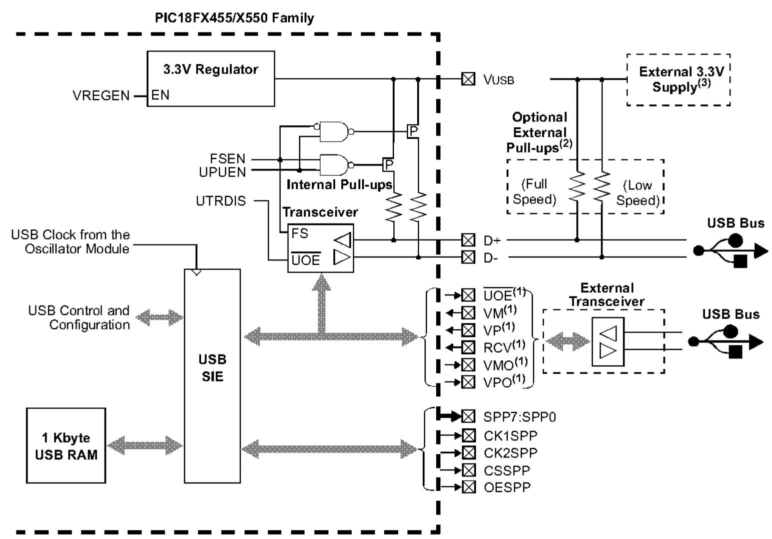

Note 1: This signal is only available if the internal transceiver is disabled (UTRDIS = 1).

2: The internal pull-up resistors should be disabled (UPUEN = 0) if external pull-up resistors are used.

3: Do not enable the internal regulator when using an external 3.3V supply.

APPENDIX D

SLSD-71N5 PLANAR PHOTODIODE

SLSD-71N5

Solderable Planar Photodiode

Features

- Visible to IR spectral irradiance range
- High reliability
- Oxide passivation
- Linear short circuit current
- Low capacitance, high speed
- Protective coating

Description

The Silonex series of silicon solderable planar photodiodes feature low cost, high reliability, and linear short circuit current over a wide range of illumination. These devices are widely used for light sensing and power generation because of their stability and high efficiency. They are particularly suited to power conversion applications due to their low internal impedance, relatively high shunt impedance, and stability. The photodiodes have a protective coating that protects them from humidity effects. These devices also provide a reliable and inexpensive detector for instrumentation and light beam sensing applications.

Absolute Maximum Ratings

Storage Temperature	-40°C to +105°C
Operating Temperature	-40°C to +105°C

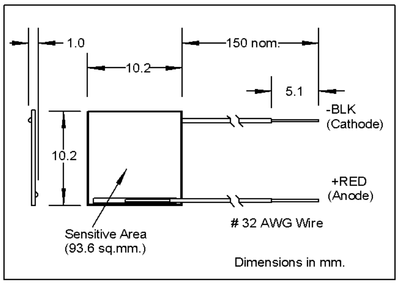

Also available without leads as part number SLCD-61N5

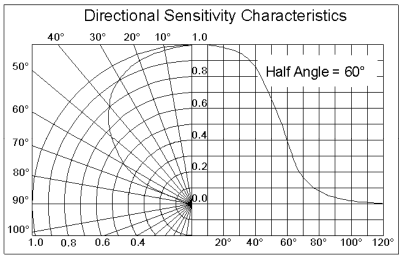

Electrical Characteristics (T_A=25°C unless otherwise noted)

Symbol	Parameter	Min	Typ	Max	Units	Test Conditions
I_{SC}	Short Circuit Current	2.5	4.0		mA	V_R=0V, Ee=25mW/cm^2 (1)
V_{OC}	Open Circuit Voltage		0.40		V	Ee=25mw/cm^2 (1)
I_D	Reverse Dark Current			3.3	μA	V_R=5V, Ee=0
C_J	Junction Capacitance		2.0		nF	V_R=0V, Ee=0, f=1MHz
S_λ	Spectral Sensitivity		0.55		A/W	λ=940nm
V_{BR}	Reverse Breakdown Voltage	20			V	I_R=100μA
λ_P	Maximum Sensitivity Wavelength		930		nm	
λ_R	Sensitivity Spectral Range	400		1100	nm	
$\theta_{1/2}$	Acceptance Half Angle		60		deg	(off center-line)

Notes: (1) Ee = light source @ 2854 °K

Specifications subject to change without notice

101420 REV 5

Northwich, Cheshire
CW9 7TN, United Kingdom
Tel: 01606-41999
Fax: 01606-49706

2150 Ward, Montreal
Que, H4M 1T7, Canada
Tel: 514-744-5507
Fax: 514-747-3906

APPENDIX E

Novel Optical Scanner Using Photodiodes Array for Two-Dimensional Measurement of Light Flux Distribution

K. K. Chong and T. K. Yew

***Abstract*—An optical scanner, also known as a flux mapping system, capable of acquiring a flux distribution pattern of a light source on a 2-D flat surface, has been designed and constructed. The novel optical scanner can measure the light flux distribution at high resolution with fewer sensors in a relatively short amount of time, and it can be used for precise calibration of any light source. The design of the optical scanner consisted of a single row of photodiodes with fixed distances that can scan and acquire flux distribution data in the 2-D measurement plane. In our prototype design of the novel optical scanner, 25 photodiodes with a photosensitive area of 1 cm^2 each were arranged in a single row and fixed to an aluminum holder. The resulting scanner was fast enough to perform scanning and recording of light irradiance over a test plane area of 1125 cm^2 within a period of 5 s.**

***Index Terms*—Contour map, flux distribution, optical scanner, photodiode array, solar simulator.**

I. Introduction

SOLAR simulators and supplemental lighting systems are widely used in research institutes and industries for indoor applications because they are readily available, their supply is consistent, and their output is not affected by the weather. For photovoltaic research, solar simulators using xenon arc lamps are widely employed to characterize the performance of solar cells by plotting I–V curves that result from the simulated sunlight. For horticulture, the use of supplemental lighting systems has significantly increased recently as more growers are interested in shortening the time needed for their crops to reach maturity and, sometimes, to increase annual yield through continuous plantings throughout the winter season [1].

In the aforementioned applications, the uniform illumination emanating from the light source in either solar simulator or supplemental lighting system is the major concern to obtain the desired outcome. Light uniformity of the solar simulator is one of the key factors to obtain accurate measurements of I–V curves for the tested solar cell [2]. Any spatial variation of light irradiance will affect the performance of solar cells and, hence, deteriorate the accuracy and consistency of the test result. On the other hand, a high degree of light uniformity is also required from a supplemental lighting system to ensure the consistency in crop yield throughout a growing area. The supplemental lighting system normally consists of light source, e.g., light bulbs, tube lamps, or arrays of light-emitting diodes, and optical components, e.g., reflectors, collimators, or filters. The main objective of the optical components is to project the light so that the irradiance from the light source can be uniformly distributed across the crops. The uniform exposure of irradiance over the crops is to avoid uneven growth and variable quality. The uniformity information can be used to determine the maximum allowable lamp spacing across the growing area. Therefore, uniformity calibration of the light source across the illuminated area in the aforementioned applications is important to quantify the quality of the light source.

In common practice, the uniformity tester utilizes a 2-D array of solar cells to assess the uniformity of irradiance on the tested surface, which is a rather expensive and complicated solution [7]. In the design of a tester, solar cells are arranged in an $m \times n$ array that covers a square or rectangular plane surface. By exposing the solar cells to the light source, a current proportional to the irradiance level will be generated by each solar cell. The signal conditioning circuitry then produces signals that are proportional to the output current and that are transmitted to the data acquisition equipment and subsequently to the computer. Finally, the computer performs data interpretation to provide a graphical display of the uniformity of the light source in a 2-D space. For the measurement over a wider surface plane, more solar cells are needed for the uniformity tester to achieve the same resolution. The size of the sensor helps in determining the resolution of the measurement system. The sensor is unable to detect the spatial nonuniformity of light irradiance within the sensor's sensitive area, and hence, the output of a larger sensor is the average irradiance of the detected light throughout its sensitive area even if there is variation of irradiance within the area. For a study or test requiring a high degree of uniformity from the light source, a reasonably small size sensor will be needed. However, this will indirectly increase the cost and complexity of the uniformity tester design. The aim of this paper is to present a design and construction of a novel uniformity tester called an optical scanner that is able to measure the distribution

Manuscript received July 20, 2010; revised January 4, 2011; accepted January 10, 2011. This work was supported in part by the Malaysia Green Technology Corporation, by the Ministry of Energy, Green Technology, and Water through the Akaun Amanah Industri Bekalan Elektrik (AAIBE) Trust Fund, and the Ministry of Science, Technology, and Innovation through the e-Science Fund. The Associate Editor coordinating the review process for this paper was Dr. Zheng Liu.

The authors are with the Faculty of Engineering and Science, Universiti Tunku Abdul Rahman, Kuala Lumpur 53300, Malaysia (e-mail: chongkk@utar.edu.my; ytkeat@yahoo.com).

Color versions of one or more of the figures in this paper are available online at http://ieeexplore.ieee.org.

Digital Object Identifier 10.1109/TIM.2011.2118850

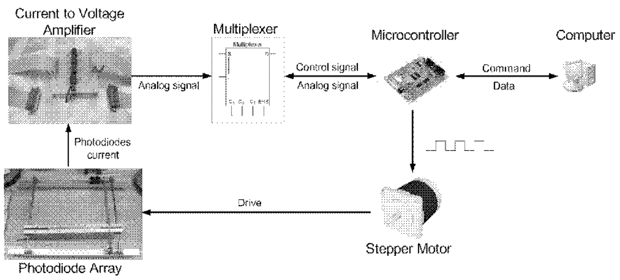

Fig. 1. Schematic showing the major components of the novel optical scanner.

of light irradiance over a plane surface with reasonably high resolution using a much simpler design.

II. Methodology

Fig. 1 shows the major components of the optical scanner. The optical scanner consists of an array of photodiodes, amplifier circuit, microcontroller, stepper motor, multiplexer circuit, and computer. The optical scanner system is controlled by the computer with a custom-designed user interface program. It is capable of sending commands to the microcontroller to perform desired functions such as to collect and to process the measurement results.

Instead of using an array of $m \times n$ photosensors, only a single row of n photodiodes is required in the novel optical scanner to measure the light irradiance across a squared or rectangular plane. This method can greatly reduce the number of sensors used and the cost of the device since the number of sensors normally accounts for a large portion of the device's cost. In addition, the high-speed scanning method of the optical scanner can allow us to map a reasonably high resolution light flux distribution pattern with a total coverage area of 1125 cm^2, where the light flux is defined as the photon energy per square meter per second with the unit of watts per square meter. The high-speed scanning can also overcome the problem of heat management of the photodiode array due to the short exposure time to the light irradiance. In the optical scanner design, the initial and final positions of photodiode array are set to be off from the illuminated area of light source so that the photodiodes are not heated up and the effect of the temperature to the measurement result can be minimized. In this case, passive cooling is sufficient by using an aluminum heat sink connected to the rear side of the photodiode array.

The resolution of the scanner is about 1 cm^2, which is equal to the photosensitive area of a single unit photodiode in the scanner. Fig. 2 shows the optical scanner with a single row of photodiodes that scans in a direction from top to bottom, and all the photodiodes are covered by a stainless-steel plate with small apertures to expose the surface of the photodiodes. The small aperture can decrease the output current as well as the heat generated from the photodiode to simplify the electronic circuit design. The square cells, as shown in Fig. 2, denote the positions at which the readings of light irradiance is acquired and subsequently sent to the microcontroller. During the process of data acquisition, the readings are collected simultaneously for all the photodiodes arranged in the same row, and then, the scanner is shifted to the next row after the readings are stored. The position and the reading of each cell are recorded by the microcontroller, and these data are sent to the computer for further processing and analysis.

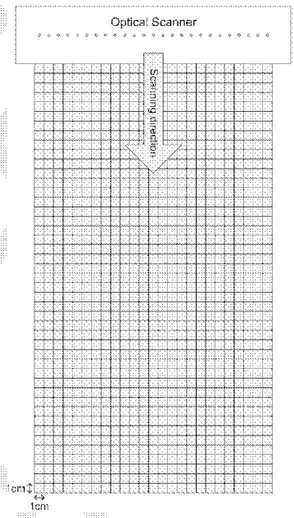

Fig. 2. Small cell representing the position and the area of each measurement during the scanning process. The square cells, as shown in the above schematic diagram, denote the positions at which the readings of light irradiance are acquired and subsequently sent to the microcontroller. During the process of data acquisition, the readings are collected simultaneously for all the photodiodes arranged in the same row, and then, the scanner is shifted to the next row after the readings are stored.

For a complete measurement, 1125 readings are taken by the photodiodes array for a plane with total surface area of

45 cm × 25 cm. The optical scanner is capable of performing one complete measurement cycle within a period of 5 s. The rapid measurement enables us to analyze the collected data almost instantaneously by plotting a flux distribution map after all the data are transferred to the computer.

A. *Optical Scanner*

In the design of the novel optical scanner, planar photodiodes were employed to detect the incoming light irradiance. The selected photodiodes respond linearly to the irradiance of the detected light over the range of 0–1000 W/m^2. The photodiodes are relatively small in size with a photosensitive area of 1 cm^2, constituting the basic pixel of the light flux distribution map. In the optical scanner, 25 photodiodes are arranged in a single row and attached to an aluminum holder to form a photodiode array. The photodiodes are arranged closely to adjacent photodiodes to avoid blank gaps that will affect the resolution of the flux distribution maps. All the photodiodes are slotted into a slot on the thin aluminum bar, and the aluminum surface beneath the photodiodes is insulated from the photodiode itself with thermal adhesive material that is thermally conductive but electrically insulated to avoid short circuiting because the output current from each photodiode had to be read separately to determine the light irradiance level at that particular pixel.

On the top surface of the photodiode array, a stainless-steel cover that contains 25 equally distant circular apertures with a diameter of 2.5 mm each is placed in such a way that each aperture is located over the center of each photodiode. The apertures located 3 mm above the photodiodes were used to block part of the diffuse component of the light so that the photodiode mainly detects the directional or beam component of the light that enters the aperture. The cover also serves as a light attenuator, and this will prevent heat from the light source to heat up the photodiodes. This approach will minimize the thermal noise that is the main contributor of signal noise to the photodiode output.

The photodiode holder was mounted on a linear slider and driven by a stepper motor via a metal chain. The shaft of the stepper motor can rotate in steps according to the step pulses generated by the microcontroller. The microcontroller generates 3000 pulses/s to drive the photodiode array at a speed of 9 cm/s. The positioning of the photodiode holder has proven to be robust, consistent, and highly accurate with negligible backslash even after many measurement runs had been performed.

Before collecting data, calibration for each individual photodiode was carried out separately to obtain the relationship between the light irradiance and photodiode output current. All the photodiodes were calibrated against a standard radiometer which provides absolute irradiance level of the light irradiance. Using the calibration information, measurements can be correlated with the absolute value of irradiance level. Fig. 3 shows the calibration graph for one of the photodiodes used in the optical scanner. All the calibration graphs show a very good linear relationship between the output current of photodiode and light irradiance since the R-squared values of all the linear graphs are higher than 0.95. Regression analysis of the graphs has been carried out to study the standard error of the regression lines. The standard errors of all regression lines have been calculated and were within the range of 2.61%–3.67% when they were compared using the error of the mean of the dependent variable. The standard errors appear to be small, and hence, the linear regression model of light irradiance as function of the photodiode current was determined to be good. The absolute value of the light irradiance detected by the photodiode used in the calibration graph as revealed in Fig. 3 can be calculated as follows:

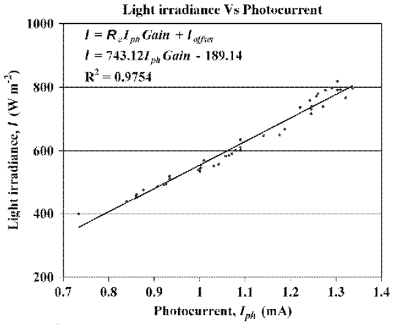

Fig. 3. Calibration graph for one of the photodiodes installed on the measurement array.

Light irradiance $\boldsymbol{I}$ (in watts per square meter)

$$= R_e \times I_{\text{ph}} \times Gain + \boldsymbol{I}_{\text{offset}}$$

where I_{ph} is the photocurrent of photodiode (in milliamperes), $Gain$ is the amplification gain of photodiode output signal, and R_e is the responsivity per unit area of photodiode, which is a constant to describe the performance of photodiode in terms of the photocurrent generated per incident optical power per unit area (in watts per square meter per milliampere), and it can be obtained from the slope of the calibration graph shown in Fig. 3 [8]. $\boldsymbol{I}_{\text{offset}}$ is a constant, and it can be obtained from the graph shown in Fig. 3 when the photocurrent output I_{ph} is 0 W/m^2.

The output signal of the photodiode can be measured as a voltage or a current. Current measurements demonstrate far better linearity, offset, and bandwidth performance. The generated photocurrent is proportional to the incident light power per unit area and can be converted to output voltage using a transimpedance configuration, also known as a current-to-voltage converter. The photodiode can be operated with or without an applied reverse bias depending on the specific application requirements. They are referred to as "photoconductive" (biased) and "photovoltaic" (unbiased) modes. For this purpose, we have configured the current-to-voltage converter in photovoltaic mode, as shown in Fig. 4.

When a photodiode is used in the photovoltaic mode, the voltage across the diode is kept at 0 V. Consequently, this almost eliminates the dark current altogether [9], [10]. Thus, the

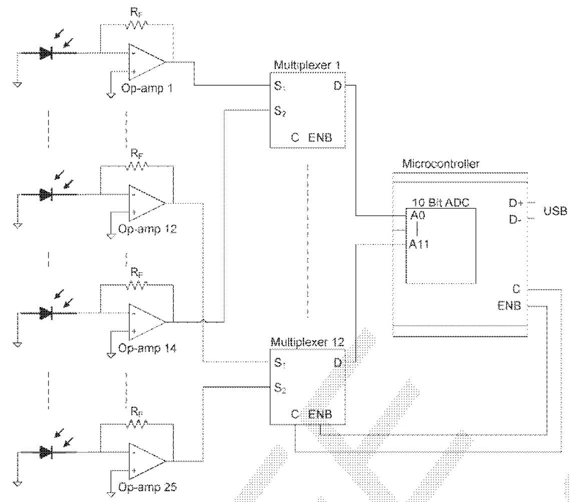

Fig. 4. Overall architecture of the photodiodes and the accompanying electronic circuit.

shot noise due to the dark current is also negligible, and thus, it increases the precision of the output signal. In addition to offering a simple operational configuration, the photocurrents in this mode have less variation in responsiveness with temperature. Although the shot noise is negligible in the photovoltaic mode, other noises found in the electronics circuit still exist including thermal noise of the photodiode, thermal noise of the feedback resistor in the amplifier, and the input offset current of the amplifier. The thermal noise of the feedback resistor and the thermal noise of the photodiode are expressed in the equations $I_N = [4kT/R_F]^{1/2}$ and $I_{\text{TH}} = [4kT\Delta f/R_{\text{SH}}]^{1/2}$, respectively, where k is Boltzmann's constant, T is the absolute temperature of the photodiode, R_F is the feedback resistance of the amplifier circuit, R_{SH} is the shunt resistance of the photodiode, and Δf is the bandwidth of the photodiode. The total calculated noise was 8.66×10^{-7} A, and the equivalent noise output voltage was 0.234 mV when it was amplified by a gain of 270. Hence, the error signal caused by the various noises was relatively small and negligible.

After converting the signals from current to voltage, the voltage signals were amplified and read by a microcontroller through a multiplexing circuit. The analog data were converted to digital data first via a 10-bit analog-to-digital converter (ADC), and the digital signals were then transferred to the computer. In the conversion, a least significant bit (LSB) represented an equivalent value of 4.88 mV, with a reference of 5 V as maximum voltage. When the equivalent value was translated into light irradiance using the calibration graph, the equivalent light irradiance value was 3.6 W/m^2. ADC conversion contains errors that are integral linearity errors, differential linearity errors, offset errors, and gain errors. The total error was 4.5 LSB or was equivalent to 16 W/m^2. The accuracy of the system is basically limited by the ADC error, so the resulting light irradiance had an accuracy in the range of ± 16 W/m^2.

The total response time of the electronic circuit and photodiode was determined by the rise time of the photodiode, slew rate of the trans-impedance amplifier, multiplexer propagation delay time, and the acquisition and conversion time of the ADC. The photodiode had a rise time of less than 4 μs. The amplifier had a slew rate of 8 V/μs of which it took 0.625 μs to increase from 0 to 5 V, representing the maximum voltage read by the optical scanner. The delay time of the multiplexer was 360 ns, and the total response time of ADC was 4.2 μs. The total maximum time to read a signal from a photodiode until the signal could be converted to a digital signal and then stored in the register was approximately 9.185 μs. Hence, it took a maximum time of 229.625 μs to complete the data acquisition process by the photodiodes array. The response time of the data acquisition system is fast enough compared to the time it took to shift the photodiode holder by 1 cm, which was approximately 111 ms.

B. Operating Procedure

Figs. 5 and 6 show the experimental setup and the operational flowchart of the optical scanner, respectively. The optical scanner is placed in the measurement plane in which the sensors surface is normal to the light beam. The process is started by sending a command from the computer to the microcontroller through universal serial bus (USB) communication. The microcontroller will check the USB communication status before starting to perform measurements. After the USB

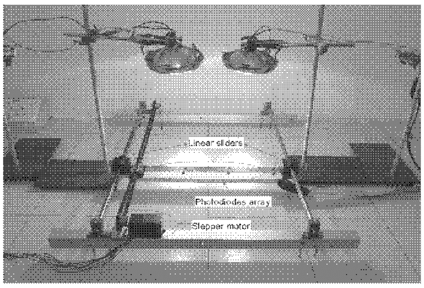

Fig. 5. Experimental setup of the optical scanner.

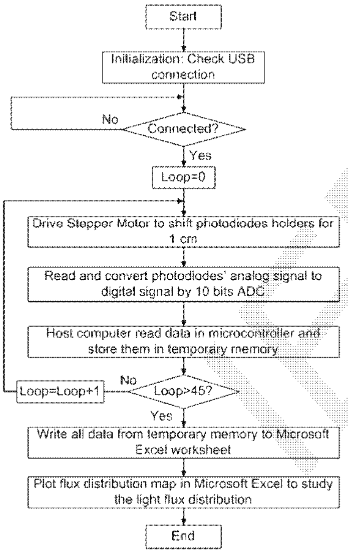

Fig. 6. Flowchart of the optical scanner operation.

connection is established, the aluminum holder will be shifted 1 cm by the stepper motor. To shift the aluminum holder, the microcontroller has to calculate the number of steps needed to run the stepper motor for 1 cm of movement. After the calculation, microcontroller will generate the required number of step pulses, and the pulses will trigger the stepper motor driver to drive the stepper motor.

For each centimeter of the photodiodes array shifted, the microcontroller will read the output signal from each photodiode through a high-speed multiplexer circuit. The analog data are then converted to 10-bit binary numbers by an ADC, and the digital data are stored in the USB communication registers of the microcontroller. After the conversion process is completed, the registers are read by the host computer. The computer will then store the data in a temporary memory array. This data collection process is repeated for 45 times, equaling the 45 cm in total distance that the sensors holder has to be moved as shown in Fig. 2. After the whole process is completed, the data stored in the temporary memory array is converted from voltage value to light irradiance value using the calibration factor obtained from the calibration graph. The irradiance values are written to a Microsoft Office Excel worksheet, and the contour map is then plotted.

III. Results and Discussion

The optical scanner has been tested to measure the light flux distribution maps of three selected light sources. The nonuniform light source is a good reference for us to test the capability of the optical scanner for detecting the variation of irradiance. The first light source tested was an artificial light source consisting of three motorcycle xenon headlamps of 35 W each. The second light source was also an artificial light source comprised of three commercial xenon lamps of 20 W each. The third light source was the sunlight with a direct normal irradiance of 752 W/m^2 as measured by a pyrheliometer. The distance between both artificial light sources and the scanner was fixed at 50 cm. All the lamps used during the measurement were reasonably new with the total operating time of less than 5 h. Fig. 7(a) and (b) shows the light distribution pattern of the first artificial light source from a picture taken by charge-coupled device (CCD) camera and a contour map generated by the optical scanner, respectively. Similarly, Fig. 8(a) and (b) reveals the light distribution patterns of the second artificial light source from a picture taken by CCD camera and a contour map generated by the optical scanner, respectively. The variation in the irradiance of the two artificial light sources can be easily identified from the contour maps with a resolution of 1 cm^2 within the measurement plane.

The measurement results of the optical scanner were compared with grayscale picture taken by the CCD camera for the same light sources during the measurement. The pictures were taken at the distance of 80 cm between the CCD camera and a black screen placed at the measurement plane of the scanner. The pictures of flux distribution patterns as shown in Figs. 7(a) and 8(a) are consistent with the measurement results obtained using the optical scanner for both position and irradiance level as shown in Figs. 7(b) and 8(b), respectively. The contour map of light flux distribution can also provide information about the absolute value of the light irradiance level. More detail about the light distribution can be accomplished by choosing a smaller range of light irradiance.

Finally, the performance of the optical scanner is also evaluated by using a highly uniform illumination source, i.e., sunlight, and therefore, the irradiance distribution of sunlight was also acquired, and the results are shown in Fig. 9. With a direct normal irradiance of 752 W/m^2, the flux distribution map in Fig. 9 has revealed that most of the measurement area exhibited irradiance levels ranging from 700 to 800 W/m^2, except a few locations. However, the overall measurement result was still

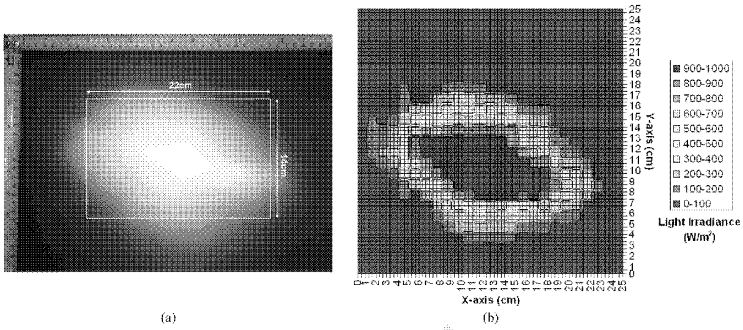

Fig. 7. Light flux distribution of the first artificial light source consisted of three motorcycle xenon headlamp of 35 W each: (a) picture taken by a CCD camera and (b) contour map plotted by the optical scanner. The light source utilized in is consisted of three motorcycle xenon headlamp with 35 W each. The distance between the light source and the scanner was fixed at 50 cm. All the lamps used during the measurement were reasonably new with a total operating time of less than 5 h.

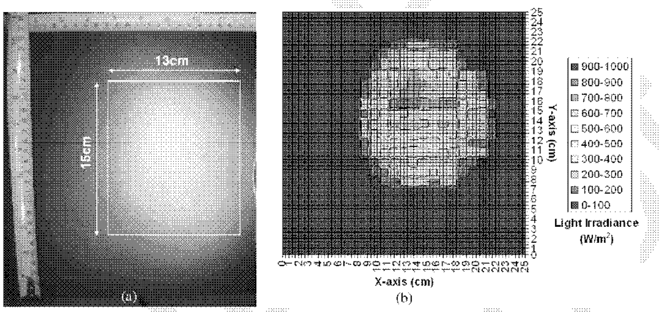

Fig. 8. Light flux distribution of the second artificial light source comprised of three commercial xenon lamps of 20 W each: (a) picture taken by a CCD camera and (b) contour map plotted by the optical scanner. The light source utilized consisted of three commercial xenon lamps of 20 W each. The distance between the light source and the scanner was fixed at 50 cm. All the lamps used during the measurement were reasonably new with a total operating time of less than 5 h.

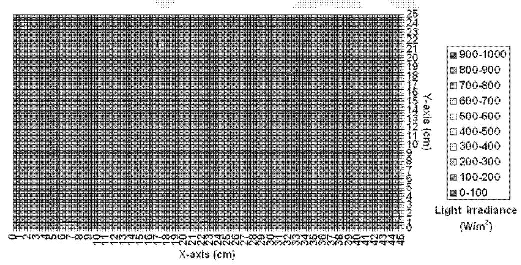

Fig. 9. Light flux distribution of sunlight with a direct normal irradiance of 752 W/m^2.

within the accuracy of the optical scanner, showing a very promising performance of the optical scanner to acquire light irradiance levels from any light source.

For the choice of aperture, there is a relationship of both the aperture distance from the photodiode and the size of aperture with the field of view of the photodiode, as illustrated in Fig. 10.

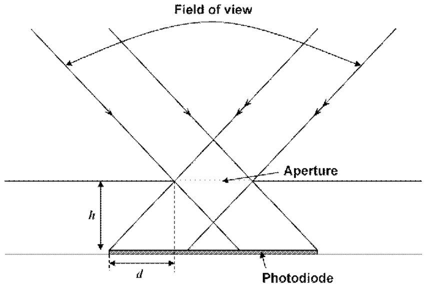

Fig. 10. Schematic diagram to show the calculation of field of view of the photodiode.

Our priority for the design of the aperture was to aim at reducing the heat absorbed by the photodiode and, thus, reduce the signal noise that can be caused by the temperature variation, as explained in Section II-A. Therefore, the field of view of our current design was 102.68°, which is less than the 160° standard required for a solar simulator. However, the current optical scanner can be easily modified to comply with the standard required for a solar simulator by reducing the distance between the aperture and the photodiode h to 0.32 mm.

The calculation of the angular of field of view is demonstrated as follows.

Field of view is defined as $\text{FOV} = 180° - 2\tan^{-1}(h/d)$, where d is the half width of photodiode minus the radius of aperture, and h is the distance between aperture and photodiode.

To calculate the field of view of our current design, $\text{FOV} = 180° - 2\tan^{-1}(3\text{ mm}/3.75\text{ mm}) = 102.68°$.

To obtain the field of view of 160°, the distance h must be further reduced from 3 to 0.32 mm, as shown in the following calculation:

$$160° = 180° - 2\tan^{-1}(h/d)$$

$$h = d\tan\theta = 3.75\text{ mm} \times \tan 10° = 0.32\text{ mm}.$$

For the tradeoffs in terms of cost, speed, accuracy, and type of light source among three different possible methods for acquiring the light flux distribution map, comparisons have been performed as shown in Table I. For the cost comparison, we estimated the cost of a stepper motor and its associated driving components to be US$312.50 and the cost of a photodiode at US$12.50. The cost estimation of the aforementioned items was based on our cost of setting up the current optical scanner.

Since the 3-D measurement device is gaining more interest in many applications now, it is also possible for the current design to be further upgraded from a 2-D to a 3-D optical scanner by adding an additional motion to the photodiode array in the vertical direction (z-axis). In this case, the data acquisition algorithm has to be modified as well to allow the data collection in three dimensions.

TABLE I
COMPARISONS IN TERMS OF COST, SPEED, ACCURACY, AND TYPE OF LIGHT SOURCE AMONG THREE DIFFERENT POSSIBLE METHODS OF ACQUIRING THE LIGHT FLUX DISTRIBUTION MAP

	Single photodetector configuration	Single row photodetector configuration	$m \times n$ array of photodetector configuration
Configuration	1 photodiode and 2 stepper motors with associated driving components	25 photodiodes and 1 stepper motor with associated driving component	1125 (or 25 × 45) photodiodes
Estimated cost (US$)	12.5 + (2 × 312.50) = 637.50	(25 × 12.5) + 312.50 = 625.00	1125 × 12.5 = 14,062.50
Data acquisition time	125 second	5 second	< 1 second
Accuracy	Lowest accuracy that is highly relied on the accuracy of 2-D motions of two stepper motors.	Moderate accuracy that is highly relied on the accuracy of 1-D motion of a single stepper motor.	Highest accuracy.
Type of light source	Stable artificial light source	All types of light sources including real time sunlight and artificial light source.	All types of light sources including real time sunlight and artificial light source.

IV. CONCLUSION

An optical scanner that is capable of plotting the light flux distribution pattern across a 2-D surface has been successfully designed and constructed. The advantage of the novel optical scanner is that it can perform direct measurement of high-resolution flux distributions in absolute irradiance levels from a light source using a fast scanning speed. The optical scanner can produce almost instantaneous results, using a scanning time of only a few seconds. The scanner can be easily scaled up by adding more photosensors and by increasing the length of the sliding bar to cover larger illumination areas. Furthermore, the current photodiodes used in the system can be replaced by different types of sensor, i.e., concentrator photovoltaic cells that respond linearly to high light irradiance so that the highly concentrated light, which is up to a thousand times the irradiance of the sun, can also be measured.

REFERENCES

[1] A. J. Both, D. E. Ciolkosz, and L. D. Albright, "Evaluation of light uniformity underneath supplemental lighting systems," *Acta Hort. (ISHS)*, vol. 580, pp. 183–190, 2002.

[2] R. Vandenberg, M. Bolingen, and R. Wieting, "What does "one-sun intensity" mean for *I–V* curve measurement? Intensity-induced errors on different types of large area a-Si modules," *Sol. Energy Mater. Sol. Cells*, vol. 29, no. 1, pp. 77–84, Feb. 1993.

[3] C. Henjes and H.-U. Frey, "Investigation on the flux uniformity depending on the lamp pattern of a solar simulator," in *Proc. 4th Int. Symp. Environ. Test. Space Programmes*, 2001, pp. 515–521.

[4] J. Coventry and A. Blakers, "Direct measurement and simulation techniques for analysis of radiation flux on a linear PV concentrator," *Prog. Photovolt.: Res. Appl.*, vol. 14, no. 4, pp. 341–352, Jun. 2006.

[5] M. Adsten, "Measurement of radiation distribution on the absorber in an asymmetric CPC collector," *Sol. Energy*, vol. 76, no. 1–3, pp. 199–206, Jan.–Mar. 2004.

[6] K.-J. Riffelmann, A. Neumann, and M. Wittkowski, "PARASCAN: A new parabolic trough flux scanner," in *Proc. ISES Sol. World Congr.*, Göteborg, Sweden, 2003.

[7] Solar Simulator Uniformity Mapper, PV Measurements, Inc., 2009. [Online]. Available: http://www.pvmeasurements.com/products/solar-simulator-uniformity-mapper
[8] S. O. Kasap, *Optoelectronics and Photonics: Principles and Practices*. Upper Saddle River, NJ: Prentice-Hall, 2001, pp. 217–253.
[9] J. Wilson, *Sensor Technology Handbook*. Amsterdam, The Netherlands: Elsevier, 2005, pp. 108–110.
[10] W. Jung, *Op Amp Applications Handbook*. Burlington, MA: Newnes, 2006, pp. 258–259.

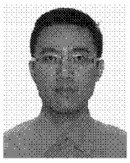

K. K. Chong received the B.Sc.(Hons.) first-class degree majoring in physics from the University of Malaya, Kuala Lumpur, Malaysia, in 1998 and the Ph.D. degree in optical engineering from Universiti Teknologi Malaysia, Malaysia, in 2002.

From 2001 to 2004, he joined the Malaysia University of Science and Technology [a collaborative program with Massachusetts Institute of Technology (MIT), Cambridge] as a Research Associate in the Institute of Energy and Environment. He is currently an Associate Professor with the Faculty of Engineering and Science, Universiti Tunku Abdul Rahman, Kuala Lumpur. His research interests include concentrating solar power, high concentrator photovoltaic systems, photovoltaic systems, nonimaging focusing technology, and solar thermal systems.

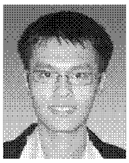

T. K. Yew received the B.Eng.(Hons.) degree in electrical engineering from the Universiti Teknologi Malaysia, Malaysia, in 2007.

He is currently a Research Assistant with the Faculty of Engineering and Science, Universiti Tunku Abdul Rahman, Kuala Lumpur, Malaysia. His research interests include optical measurement systems, high concentrator photovoltaic systems, and nonimaging focusing technology.